Analysis of Debris Signature Characteristics and Evolution in the 24 May 2016 Dodge City, Kansas, Tornadoes

ZACHARY B. WIENHOFF,[a,e] HOWARD B. BLUESTEIN,[a] DYLAN W. REIF,[a] ROGER M. WAKIMOTO,[b] LOUIS J. WICKER,[c] AND JAMES M. KURDZO[d]

[a] *School of Meteorology, University of Oklahoma, Norman, Oklahoma*
[b] *Department of Atmospheric and Oceanic Sciences, University of California, Los Angeles, Los Angeles, California*
[c] *NOAA/OAR/National Severe Storms Laboratory, Norman, Oklahoma*
[d] *Lincoln Laboratory, Massachusetts Institute of Technology, Lexington, Massachusetts*

(Manuscript received 19 May 2020, in final form 12 October 2020)

ABSTRACT: On 24 May 2016, a supercell that produced 13 tornadoes near Dodge City, Kansas, was documented by a rapid-scanning, X-band, polarimetric, Doppler radar (RaXPol). The anomalous nature of this storm, particularly the significant deviations in storm motion from the mean flow and number of tornadoes produced, is examined and discussed. RaXPol observed nine tornadoes with peak radar-derived intensities (ΔV_{max}) and durations ranging from weak ($\sim$60 m s^{-1}) and short lived (<30 s) to intense (>150 m s^{-1}) and long lived (>25 min). This case builds on previous studies of tornado debris signature (TDS) evolution with continuous near-surface sampling of multiple strong tornadoes. The TDS sizes increased as the tornadoes intensified but lacked direct correspondence to tornado intensity otherwise. The most significant growth of the TDS in both cases was linked to two substantial rear-flank-downdraft surges and subsequent debris ejections, resulting in growth of the TDSs to more than 3 times their original sizes. The TDS was also observed to continue its growth as the tornadoes decayed and lofted debris fell back to the surface. The TDS size and polarimetric composition were also found to correspond closely to the underlying surface cover, which resulted in reductions in Z_{DR} in wheat fields and growth of the TDS in terraced dirt fields as a result of ground scouring. TDS growth with respect to tornado vortex tilt is also discussed.

KEYWORDS: Supercells; Tornadoes; Radars/Radar observations; Remote sensing

1. Introduction

For over 30 years, mobile-Doppler radars have provided higher spatiotemporal resolution datasets than are generally attainable with the Weather Surveillance Radar-1988 Doppler (WSR-88D) instruments (e.g., Alexander and Wurman 2005; Biggerstaff et al. 2005; Bluestein and Pazmany 2000; Bluestein et al. 1995, 2007; Kurdzo et al. 2017; Wakimoto et al. 2018, 2020; Wurman et al. 1997). Mobile radars not only add the benefit of higher-resolution data, but they also allow for planning and prepositioning of the platforms such that the chances of observing severe convective storms are maximized.

More recently, rapid-scan capabilities have been added to mobile-radar platforms, further improving the quality of data collection. Rapid-scanning capabilities have been previously shown to be important to the collection of tornado data given the rapidly evolving nature of their small-scale features (e.g., Bluestein et al. 2010). To date, there are only a handful of mobile radars capable of scanning "rapidly" (volumetric update times of $\ll$1 min), such as the rapid-scan Doppler on Wheels (Wurman and Randall 2001), the rapid-scan, X-band, polarimetric Doppler radar (RaXPol; Pazmany et al. 2013) and the Atmospheric Imaging Radar (AIR; Isom et al. 2013), with additional platforms becoming available in the near future [e.g., Polarimetric AIR (PAIR); Salazar-Cerreno et al. 2017].

In addition, the upgrade of many radars, both mobile and fixed-site, to dual-polarization has given us the ability to also study microphysical characteristics of tornadic storms (e.g., Kumjian and Ryzhkov 2008; Mahre et al. 2018; Snyder and Bluestein 2014; Snyder et al. 2010, 2013). Polarimetric upgrades have also allowed for additional studies of tornadoes and their debris signatures (TDS; Ryzhkov et al. 2005, 2002). Many of these studies have examined the behaviors of TDSs with respect to changes in the tornado, and have attempted to link their existence to changes in both tornado- and storm-scale processes (e.g., Bodine et al. 2014; Griffin et al. 2020; Houser et al. 2015, 2016).

On 24 May 2016, a supercell thunderstorm produced 13 total tornadoes over an approximately 90-min period on the south and west sides of Dodge City, Kansas. Nine of these tornadoes were sampled at close range by RaXPol during three separate deployments (Table 1), which documented the entire life cycles from seven of the tornadoes. Although many of the tornadoes were weak and short lived, several strong tornadoes (EF2 or greater on the enhanced Fujita scale) were observed and documented, each of which occurred with different mesocyclones (four complete mesocyclone "cycles" are observed in total).

The work presented herein has two primary objectives. First, the sequence of storm-related events on 24 May 2016 will be discussed in detail. This case study will discuss multiple cases of

[e] Current affiliation: Wind Engineering Research Laboratory, Department of Civil and Environmental Engineering, University of Illinois at Urbana–Champaign, Urbana, Illinois.

Corresponding author: Zachary B. Wienhoff, wienhof1@illinois.edu

DOI: 10.1175/MWR-D-20-0162.1

TABLE 1. List of RaXPol deployments on 24 May 2016.

Deployment	Time	Scanning strategy	Location
1	2314–2346 UTC	2313–2315: 0°–20°/2°, 75-m range resolution 2315–2318: 0°–10°/1°, 30-m range resolution 2319–2342: 0°–6°/1°, 30-m range resolution 2342–2346: 0°–10°/1°, 30-m range resolution	9.5 km south of Dodge City
2	2356–0007 UTC	2356–2357: 0°–10°/1°, 30-m range resolution 2357–0007: 1.5°, 30-m range resolution	3.2 km south of Dodge City
3[a]	0055–0117 UTC	0055–0117: 0°–20°/2°, 75-m range resolution	2.4 km west-southwest of Kinsley, Kansas

[a] Deployment 3 occurred east of Dodge City on a separate supercell, which produced cyclonic and anticyclonic tornadoes. These observations will be discussed in a future study.

tornadogenesis that were observed to occur within one storm, similar to the studies of the 2007 Greensburg, Kansas, tornado study by Tanamachi et al. (2012). Thus, these tornadoes can be compared with each other, specifically examining the characteristics of their intensities (i.e., ΔV_{max}) and how they changed as the tornado formed, matured, and weakened, and then compared with previous studies (e.g., French et al. 2014). Second, a study of tornado debris is presented, focusing on the growth and decay of the TDS with respect to changes in the tornado intensity and width and near-storm environment, similar to the in-depth TDS studies of Van Den Broeke (2015). We will attempt to build on previous studies through the analysis of debris ejections, which have been shown previously to cause rapid expansion of TDSs (Kurdzo et al. 2017; Houser et al. 2016), and are linked to storm-scale rear-flank-downdraft (RFD) surges. In addition, we will examine changes in the TDS as potentially related to both ground cover and vortex tilt, on which little work has been done previously.

The following section provides further details about the radar instrumentation and method used in this study. Section 3 provides a brief description of the synoptic-scale environment on 24 May 2016. A detailed description and analysis of the event as observed by RaXPol are in section 4, and section 5 includes the analysis of the tornado debris signatures. Section 6 discusses some of the mechanisms responsible for the observed changes in TDS size, and several new, unexplored causes of TDS expansion are proposed and discussed. Section 7 summarizes the work and offers several avenues for further exploration.

2. Instrumentation and methods of data collection

The study herein stems from two sources of radar data: RaXPol and the Dodge City S-band (10-cm wavelength) WSR-88D.

a. The RaXPol mobile radar

The RaXPol mobile radar is a rapidly scanning, polarimetric, mobile radar operating at 3-cm (X band) wavelength. RaXPol is capable of mechanically scanning at a rate of $180° s^{-1}$, making it one of the most rapidly updating nonphased-array radar platforms, and it was utilized throughout the entirety of this event. Because RaXPol spins so rapidly, a frequency-hopping technique is employed to allow the platform to collect a larger number of independent samples in a shorter time than would have been possible without frequency hopping. In addition, RaXPol is capable of higher spatial resolution than most phased-array platforms, offering a 3-dB half-power beamwidth of 1°, which increases to an effective beamwidth of ~1.4° when scanning at maximum speed because of beam smearing (e.g., Bluestein et al. 2010). Additional details about RaXPol can be found in Pazmany et al. (2013).

On 24 May 2016, RaXPol collected data for approximately 10 tornadoes during three deployments. This paper will focus largely on deployment 1 (D1; "D" refers to the individual deployments listed in Table 1) in the Dodge City supercell, for which the majority of the tornadoes (nine) were observed, but D2 will be briefly examined as well. During D1, volumetric data were collected mostly in "tornado" mode, for which shallow volumes spanning only from 0° to 6° in 1° increments were used and a range resolution of 30 m was used to maximize spatial resolution in the tornado, resulting in volumetric updates of less than 20 s. At the beginning and end of D1, when the supercell was still at a moderate distance (>10 km) from RaXPol, deeper volumes (0°–10° and 0°–20° in 1° and 2° increments) with coarser range resolution (75 m) were collected to increase radar sensitivity at longer range. All data were manually dealiased using "SOLO3" (Oye et al. 1995).

b. The Dodge City WSR-88D

The Dodge City WSR-88D, KDDC, provided supplemental data for observing periods when RaXPol was not collecting data. KDDC (and all of the WSR-88Ds) scan at the rate of $30° s^{-1}$, resulting in volumetric updates every 4–6 min. Recent upgrades to the network's scanning strategies allow for more frequent data collection at the lowest levels, if desired, by revisiting the lowest two or three elevations intermittently during a single volume [e.g., Supplemental Adaptive IntraVolume Low-Level Scan (SAILS), MESO-SAILS (SAILS x3), etc.; https://www.roc.noaa.gov/]. A range-gate spacing of 250 m is used with a radial spacing of 0.5°, which is oversampled from the half-power beamwidth of 1° (known as "super-resolution"; Torres and Curtis 2006).

3. Synoptic overview

Much of the central United States experienced an active period of severe weather during the final 10 days of May 2016. On 24 May, a midlevel shortwave ejected northeastward over the central high plains (Fig. 1). In response to the ejecting trough, a deepening lee cyclone resided in southeastern Colorado–southwestern Kansas, which propagated across into western Kansas during the

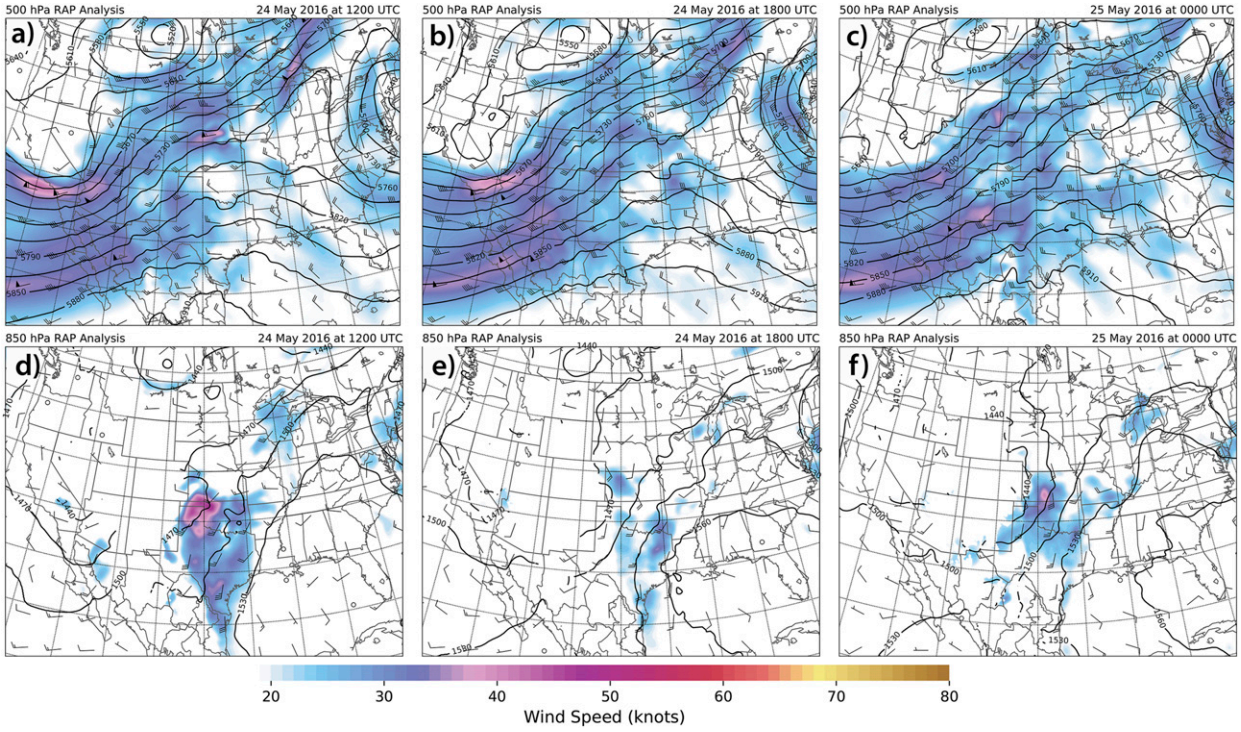

FIG. 1. Synoptic overview of the 24 May 2016 tornado event, showing (top) 500- and (bottom) 850-hPa analyses at (a),(d) 1200; (b),(e) 1800; and (c),(f) 0000 UTC. The geopotential heights (m; solid black lines) as well as the wind barbs and color-contoured wind speed (kt; 1 kt $\approx$ 0.5 m s^{-1}) are plotted at each level.

afternoon of 24 May. In addition, in response to the deepening cyclone, an 850-hPa southerly low-level jet had overspread much of the Texas and Oklahoma Panhandles and western parts of Kansas and Oklahoma (Figs. 1d–f).

At the surface, a dryline extending southward into the Texas Panhandle (Fig. 2c) helped to promote convection initiation during the early afternoon hours, serving as a focus for near-surface convergence. As an MCS originating in the Kansas Interstate (highway)-70 corridor during the early morning hours of 24 May propagated southeastward across Kansas, a convective outflow boundary pushed south and southwestward, eventually stalling across southwestern Kansas and northern Oklahoma (Figs. 2a–c). A special 1800 UTC sounding (Fig. 2d) from KDDC, which was nearly collocated with the outflow boundary at the time, revealed a "loaded gun" thermodynamic profile with CAPE in excess of 4000 J kg^{-1}, and modest CINH values. In addition, supercell-supporting deep-layer shear in excess of 20 m s^{-1} (e.g., Rotunno and Klemp 1982, 1985) combined with substantial near-surface hodograph curvature resulted in an environment supportive of supercells and, possibly, strong tornadoes (Thompson et al. 2002, 2007).

4. Examination of storm evolution

a. Storm initiation and genesis of tornado 1

By early afternoon on 24 May, storms began to develop in southwestern Kansas near the triple point, the intersection of the dryline and residual outflow boundary. Convection initiation was evident by ~2130 UTC as based on KDDC radar[1] (Figs. 3a,b) near and just to the east of the outflow boundary (Fig. 3, white dashed line). By 2230 UTC, numerous storms initiated near the triple point and grew into a cluster of supercells, most of which moved ENE. However, a quasi-isolated storm that formed to the south of Dodge City began to ingest the outflow boundary, which became evident as the radar fine line developed an obvious "kink" collocated with the supercell's inflow notch (Fig. 3e, white dot–dashed line). As the storm approached maturity, it began to propagate northward along the boundary, which was pulled northward by the storm over time. Figure 3 illustrates the outflow boundary motion (white dot–dashed line) in which the initially east-southeastward-oriented boundary segment shifted northward, remaining collocated with the supercell throughout. At 2250 UTC, the storm began producing a tornado southwest of Dodge City, the first of many on that day.

b. RaXPol observations

RaXPol's first deployment (D1) began just before 2314 UTC approximately 9 km south of Dodge City. Figure 4 provides a visual overview of each of the 13 tornado tracks observed[2] on

[1] Prior to convection initiation, at least four wind farms were visible on KDDC. These have been highlighted in Fig. 3a so as to avoid potential confusion about the time of convection initiation.

[2] All tornado tracks in Fig. 4 were either visually or radar confirmed (i.e., $\Delta V_{max} > 60$ m s^{-1}) via RaXPol data unless otherwise noted.

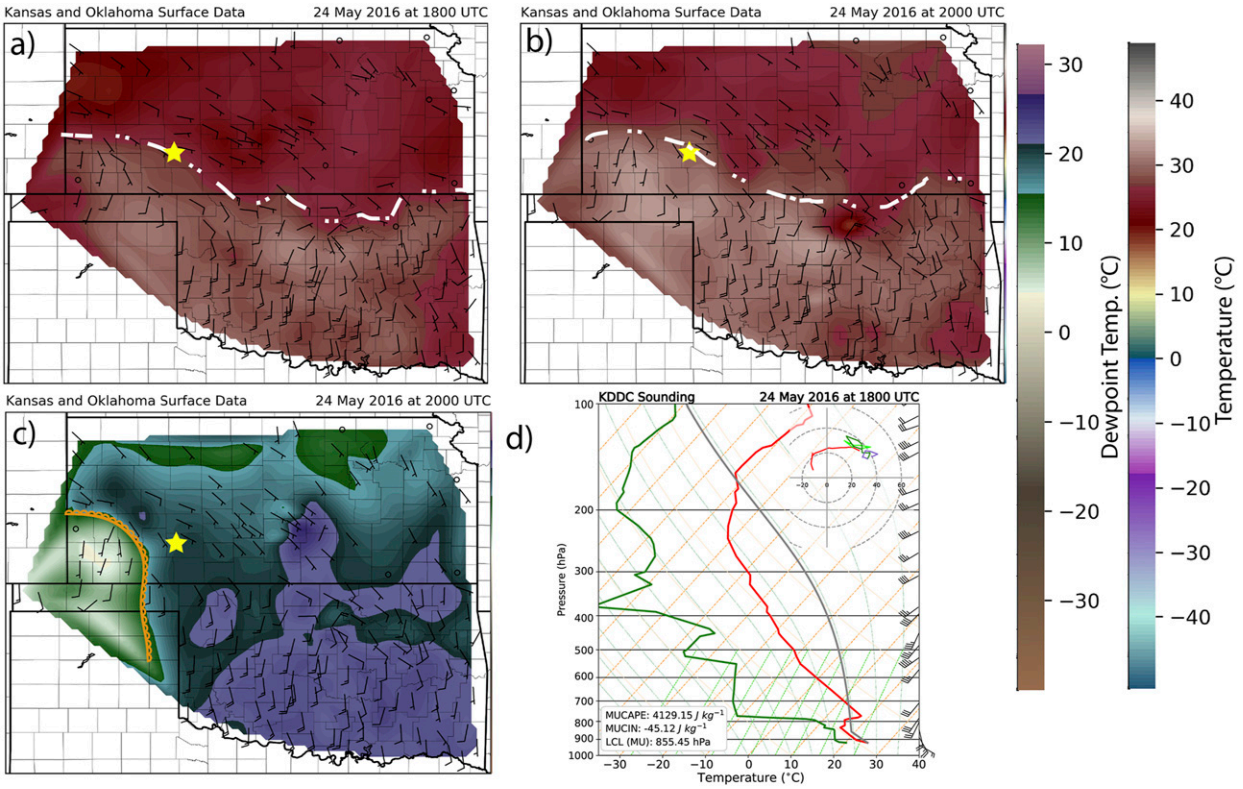

FIG. 2. Surface temperature maps at (a) 1800 and (b) 2000 UTC and surface dewpoint at (c) 2000 UTC, along with a special sounding launched by the Dodge City Weather Forecast Office at (d) 1800 UTC. In (a)–(c), temperatures (°C) are color contoured with wind barbs overlaid. The yellow star denotes the location of the sounding launch in (d). The white dot–dashed line marks the edge of a residual outflow boundary (OFB) that was located near the Oklahoma–Kansas border for much of the day. The dryline location is denoted by the scalloped orange line in (c).

this day. Each tornado is color coded by the mesocyclone with which it was associated as the storm cycled *at least* four separate times during its life. Each mesocyclone cycle was responsible for at least one tornado, and each mesocyclone produced at least one significant tornado.

At the beginning of data collection, the mature tornado 1 was approximately 10 km to the west of RaXPol and had already begun to develop a westerly component to its track, left of its initially northward translation. In addition, a new area of rotation was developing to the east of the original, or just over 5 km to the west of RaXPol (Fig. 5a). Figure 6 provides visual illustration as viewed from RaXPol during D1. By 2320 UTC, the maximum differential velocity of tornado 1 decreased from in excess of 140 m s^{-1} to approximately 100 m s^{-1}, and the tornado became visually obscured from the viewpoint of RaXPol as it became increasingly encased in rain (Fig. 6b). Analysis of tornado intensities via the maximum differential velocity $\Delta V_{\max}$ across the tornado vortex signature is provided in Fig. 7, with each panel corresponding to the associated mesocyclone cycle (only mesocyclones 1, 2, and 3 were sampled by RaXPol). Although data collection was initially sporadic in D1 because of modifications in scanning strategy, the evolution of the tornado's intensity remains intact despite analysis gaps. When RaXPol began sampling tornado 1, it was a strong tornado with near-surface $\Delta V_{\max}$ ranging from 125 to 150 m s^{-1}. The tornado generally exhibited a relative minimum in intensity from just above the surface through ~1–1.5 km, above which it was stronger. This observed minimum is similar to those discussed by Houser et al. (2015, see their Fig. 12) where a relative minimum in the tornado's intensity was observed at 1.5 km AGL in the early stages of the El Reno, Oklahoma (2011), tornado. In that case, the authors hypothesized that the initial weakness was the result of a capping inversion between 1.5 and 3 km AGL, which was also present in this case (Fig. 2d). This explanation makes physical sense given that the inversion would act to suppress the component of vertical motion due to positive buoyancy, and therefore preventing some degree of stretching in this region of the vortex. Alternatively, the minimum could be a symptom of the superposition of the low- and midlevel vortices, consistent with the explanations of Bluestein et al. (2019). Vertical motions within the column induced by the perturbation pressure gradient force in the low-level vortex and buoyancy-induced vertical motions above the LFC are not continuously increasing, such that the vertical derivative of vertical velocity becomes slightly negative. Divergence within this layer of the column results in a slight reduction of vertical vorticity, and therefore a relative minimum in $\Delta V_{\max}$. This low-level relative minimum persisted throughout the period in which tornado 1 was most intense (~2320 UTC),

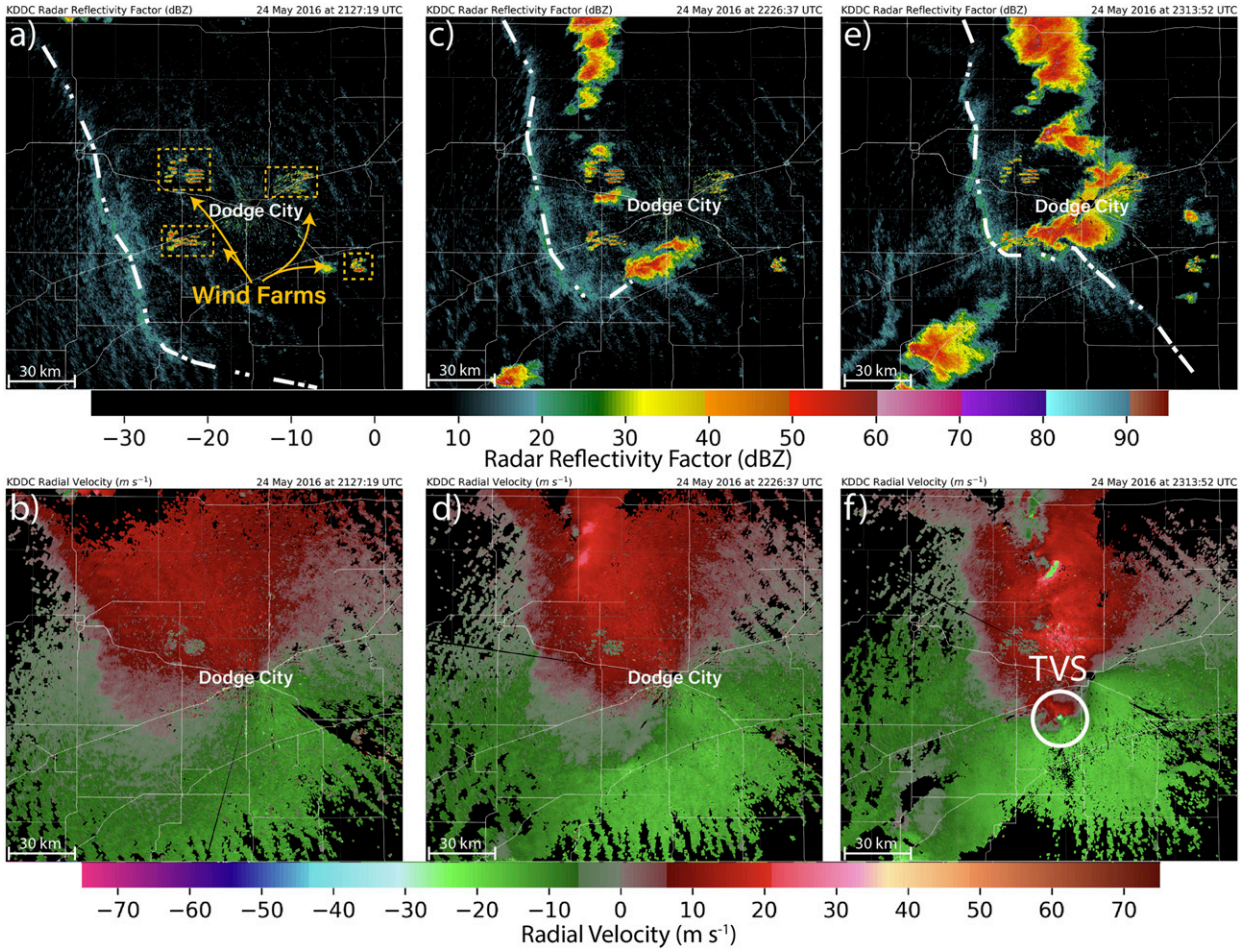

FIG. 3. (top) Radar reflectivity and (bottom) radial velocity from the Dodge City WSR-88D at (a),(b) 2127:19; (c),(d) 2226:37; and (e),(f) 2313:52 UTC. The white dashed line denotes the location of a residual OFB, which served as a focus for convection initiation by ~2200 UTC. By 2313:52 UTC[(e) and (f)], a supercell and hook echo were observed, and the OFB can be seen bending back into the storm. The location of the tornado vortex signature (TVS) is noted in (f). Wind farms surrounding Dodge City are indicated in (a) to differentiate wind turbine echoes from echoes of developing convection.

although RaXPol volume scans focus only on low elevation scans (below 6.0°) after 2320 UTC, and therefore the re-intensification of the vortex aloft may have persisted and not have been sampled.

After 2320, the tornado steadily weakened to below 100 m s^{-1}, first aloft and then near the surface, consistent with previous studies (French et al. 2013; Griffin et al. 2019; Houser et al. 2015). From visual observation and ground and aerial damage survey, it was found that tornado 1 dissipated shortly before 2324 UTC, which is also corroborated in the ΔV_{max} analysis. In this case, a minimum ΔV_{max} threshold of 60 m s^{-1} was used (Fig. 7—see color scale) simply given that it provided the most consistent agreement between visual observations, observations of damage, and RaXPol data. Previous studies have used a range of different ΔV_{max} thresholds, ranging from 20–30 m s^{-1} for studies utilizing imaging/phased array platforms with larger effective beam widths (e.g., Griffin et al. 2019; French et al. 2013), to 40 m s^{-1} (Alexander and Wurman 2008), to 55 m s^{-1} for mechanically scanning radars like RaXPol sampling the tornado at close range (Houser et al. 2015). Tanamachi et al. (2013) also approximated the minimum ΔV_{max} necessary to produce a condensation funnel to be greater than 40 m s^{-1} in several cases on the basis of crude analyses of the dynamic pressure drop at the center of several tornadoes.

As tornado 1 weakened to less than 60 m s^{-1}, the subsequent strengthening of the second mesocyclone to tornado strength east of the first began to produce a number of small, short-lived tornadoes. Tornado 2 occurred just prior to D1 and was not sampled. RaXPol sampled tornado 3 at 2314:39; this tornado was due east of tornado 1. Although short lived, the analysis in Fig. 7 indicates the sporadic presence of ΔV_{max} from greater than 60 m s^{-1} during short periods at the beginning of D1 prior to major intensification of the mesocyclone to greater than 100 m s^{-1} several minutes later. Tornado 4 was visually observed from the location of RaXPol (Fig. 6b) and exhibited a $\Delta V_{max} > 60$ m s^{-1}, despite also being very short lived (less than 30 s).

During its early evolution, initial tornadoes produced by mesocyclone 2 were weak and short lived, all of which

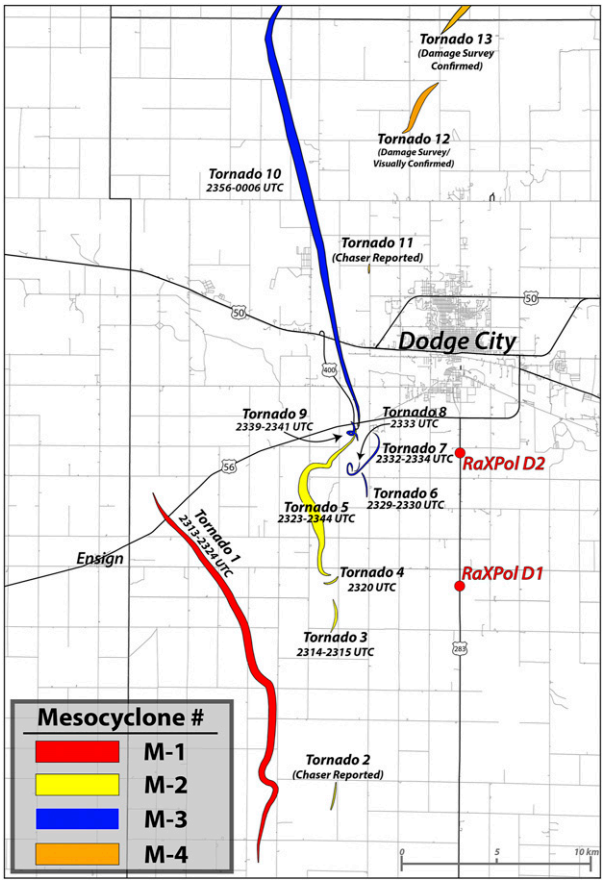

FIG. 4. Compiled map of an estimated 13 total tornadoes produced on 24 May 2016 near Dodge City. A total of 9 tornadoes (1, 3, 4, 5, 6, 7, 8, 9, and 10) were documented via RaXPol data, and a 10th was confirmed visually by the RaXPol crew en route to deployment 3. Tornadoes 2, 11, and 13 were confirmed via a combination of spotter reports, WSR-88D data, and poststorm damage surveys by the National Weather Service in Dodge City. The tornadoes are color coded by the mesocyclone cycle from which they were produced.

exceeded a ΔV_{max} of 60 m s^{-1} but never exceeded 80 m s^{-1}. In the two tornadoes (tornadoes 3 and 4) sampled by RaXPol, the ΔV_{max} sampled near the ground surpassed 60 m s^{-1} in the lowest levels but was notably weaker at upper elevations (RaXPol was only sampling up to 6° during this time). Although these vortices were associated with mesocyclone 2, we hypothesize that weakness in the low- to midlevel mesocyclone 2 sampled by RaXPol lacked the support from aloft necessary to generate more long-lived vortices. A dual-Doppler analysis using data from RaXPol and KDDC[3] illustrates the presence of the outflow boundary (Fig. 8, black dot–dashed line), denoted by an obvious weakening of the surface wind field on the south and southwest side of the mesocyclone (Fig. 8c). Meanwhile, weak low-level vertical velocities (1 km) atop the surface vorticity likely acted to stretch this vorticity, producing several of these vortices during the storm's lifetime (e.g., Fig. 8d). This process occurred on several occasions during immature stages of mesocyclone 3, which is illustrated in Fig. 8d. Early (2317:21 UTC), the strongest vertical velocities were concentrated about the periphery of the vertical vorticity maximum, with a streamer of weaker vertical vorticity along the forward flank. With time (after 2321 UTC), this vertical velocity maximum that was initially only located on the periphery of the vertical vorticity maximum became wrapped into the inflow notch as mesocyclone 2 intensified and became the new, dominant mesocyclone and updraft. As this occurred, the vertical vorticity maximum continued to strengthen to greater than 8×10^{-2} s^{-1}, and a hook echo began to accompany the vorticity maximum after 2325 UTC, approximately the time at which genesis of tornado 5 occurred (Figs. 8a–c).

As the mid- and upper-level mesocyclone intensified, tornado 5, the second significant tornado produced by this storm, began shortly after 2325 UTC (Fig. 7). Despite the presence of relatively strong ΔV_{max} (>60 m s^{-1}) near the ground throughout a prolonged period, the production of tornado 5 did not occur until an amplification in ΔV_{max} aloft to greater than 80 m s^{-1} was observed, which also began after 2324 UTC.

From tornadogenesis through approximately 2334 UTC, the tornado continued intensifying at all sampled levels, with peak $\Delta V_{max} > 150$ m s^{-1} observed in the lowest RaXPol tilts (i.e., 0° and 1° tilts). Although tornado 5 was still approaching peak intensity prior to 2330 UTC, the storm was beginning to again show signs of cyclic mesocyclogenesis, evident in both single- and dual-Doppler radar analyses. RaXPol data at 2329:16 UTC show a TVS with a $\Delta V_{max} > 103$ m s^{-1} to the northwest closely located near another weak tornado (tornado 6; peak ΔV_{max} of 66.5 m s^{-1}) that was associated with the third mesocyclone in the sequence (Fig. 5b). Dual-Doppler analysis (Fig. 8d) shows intensification of a second low-level vorticity maximum to greater than 5×10^{-2} s^{-1} on the northeast of tornado 5's location along both a "wrapped in" vertical velocity maximum and the surface boundary, a favorable region for intensification of the new mesocyclone (mesocyclone 3). As tornado 5 reached peak intensity (>153 m s^{-1}), two additional tornadoes were produced coincident with mesocyclone 3. At 2333 UTC, three tornadoes including tornado 5 were visible from RaXPol (Fig. 6c), with tornadoes 7 and 8 also exhibiting the same behavior as the previous three short-lived vortices. Figure 5c shows tornado 5, with ΔV_{max} greater than 150 m s^{-1} on the southwest side of the two tornadoes, both located within the same region of larger-scale rotation. In accordance with the single-Doppler RaXPol data and visual observations, tornado 7 began on the eastern side of the strengthening mesocyclone and tracked counterclockwise around the mesocyclone before moving more rapidly off to the northeast. Figure 4 shows the irregular track of tornado 7 with respect to tornadoes 5 and 8. Meanwhile, as tornado 7 was following an irregular track around the mesocyclone, tornado 8 formed, again on the eastern periphery of the mesocyclone.

[3] Dual-Doppler analyses were produced using a spatially variable advection correction technique, which allows for proper temporal matching between the slower-scanning WSR-88D and the rapid-scanning RaXPol. More information on the dual-Doppler method is presented in Wienhoff et al. (2018) and in the appendix.

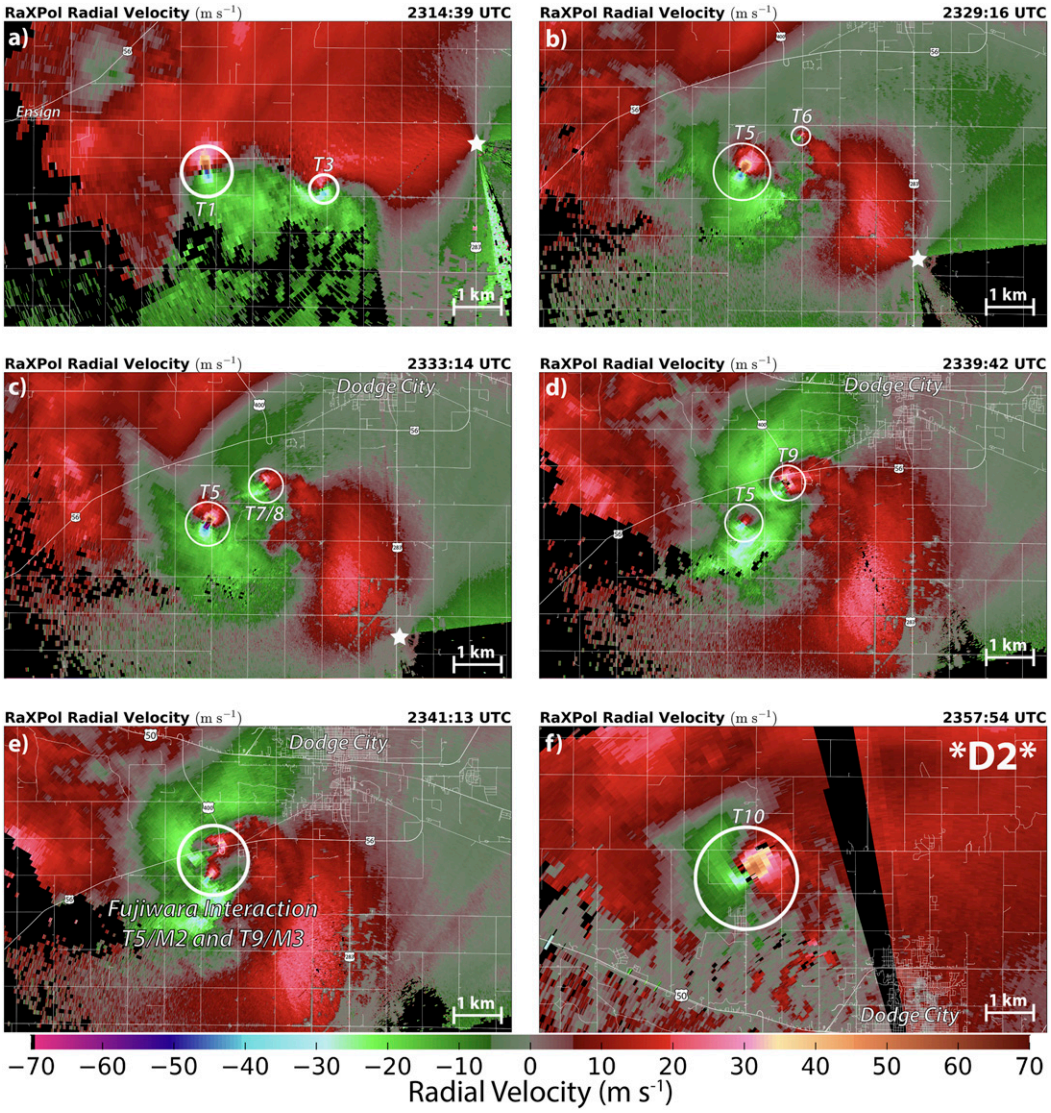

FIG. 5. Select RaXPol radial velocity images highlighting the tornado vortex signatures at (a) 2314:39, (b) 2329:16, (c) 2333:14, (d) 2339:42, (e) 2341:13, and (f) 2357:54 UTC. The tornado number corresponding to each TVS is indicated in each panel. The white star represents the location of RaXPol in (a)–(c). All data were collected during D1 unless otherwise indicated.

Although the dual-Doppler analysis begins to show intensification of the third mesocyclone at 2325:19 UTC (Fig. 8c), it is not until approximately 4 min after (2329 UTC) that the first tornado was produced by mesocyclone 3. Between 2329 UTC and 2339 UTC, the mesocyclone remained relatively weak, fluctuating above and below tornado strength (60 m s^{-1}). In the cases of tornadoes 6–8, a $\Delta V_{max} > 60$ m s^{-1} is observed for a short period during tornado 6 (~30 s), and a longer period (~90 s) during tornados 7 and 8,[4] although the strongest tornado of the three peaked in sampled intensity at 67.5 m s^{-1}. As mentioned previously in regard to the short-lived tornadoes in mesocyclone 2, the sampled ΔV_{max} aloft remains below tornado strength, again suggesting that these vortices were most likely a result of surface-based vorticity being stretched by low-level convergence, but without sufficient upper-level "support" of the primary updraft/mesocyclone to generate a longer-lived tornado vortex.

Tornado 5 continued its general progress northward as a strong tornado through ~2338 UTC (Fig. 4). As it did, ΔV_{max} remained largely steady and in excess of 105–120 m s^{-1} at all levels. At approximately 2336 UTC, ΔV_{max} aloft (i.e., 5° and 6° RaXPol elevations) began to weaken, and propagated downward to the surface. By 2338 UTC, the weakening aloft began

[4] Although tornado 8 was observed by RaXPol simultaneously with tornado 7 under mesocyclone 3, at no point was it ever stronger than tornado 7. Therefore, its time span is denoted in Fig. 7c, but its intensity never contributes to ΔV_{max}.

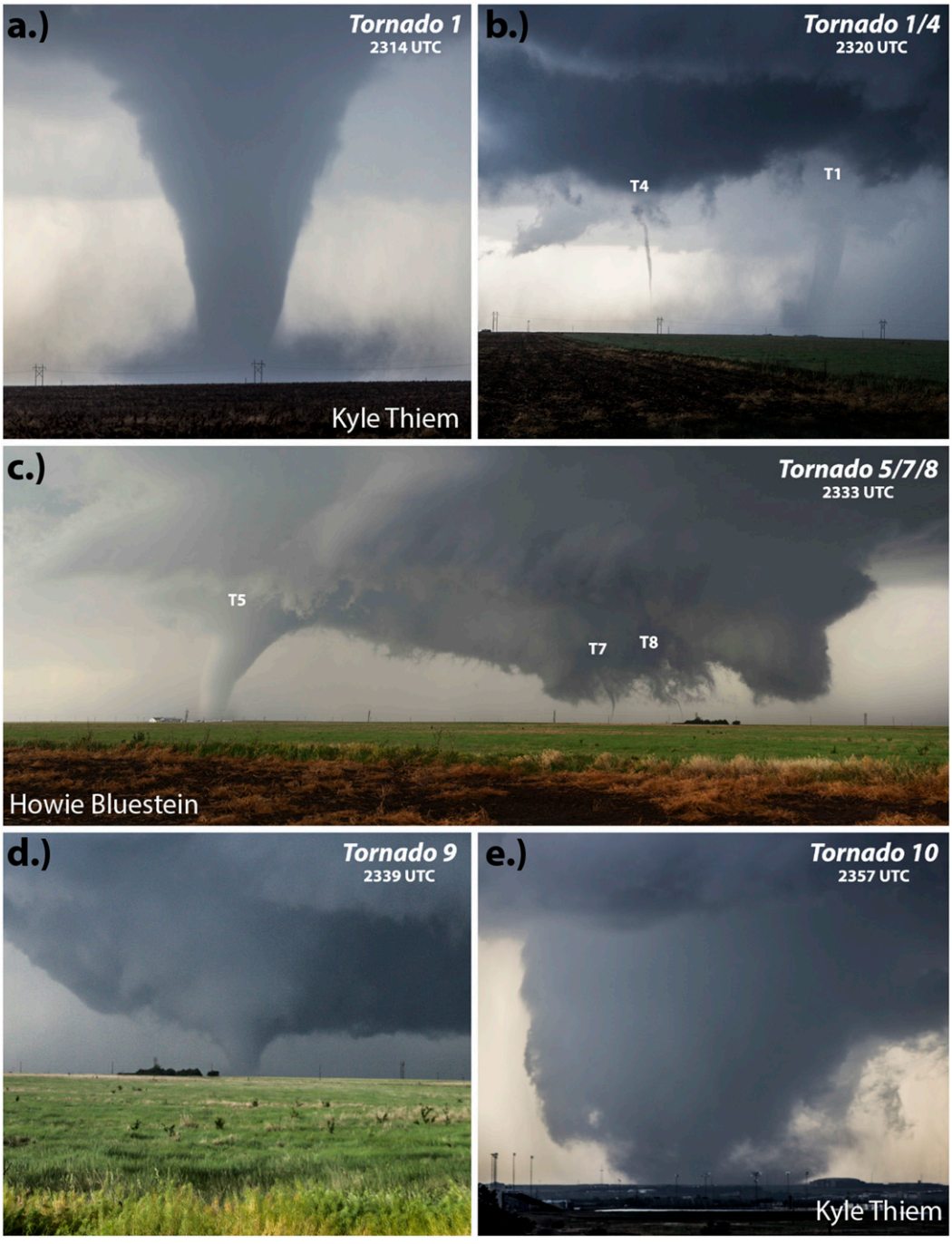

FIG. 6. Photographs of seven of the Dodge City tornadoes as observed from the location of RaXPol. Radar data from both RaXPol and KDDC, along with photographs and damage survey analyses, were used to reconstruct and document the number of tornadoes produced during the event. All photographs except that of tornado 10 were taken from RaXPol deployment 1 location by the first author unless otherwise noted.

to manifest itself near the surface, and there was a sudden change in the tornado's track. The RaXPol-derived tornado tracks in Fig. 4 show tornado 5 making a sharp right to the northeast and narrowing as it began to approach U.S. Route 56, similar to the observations by French et al. (2014) during the decay phase of the Kingfisher, Oklahoma, and Goshen County, Wyoming, tornadoes. As mesocyclone 3 continued to intensify, interaction between mesocyclones 2 and 3 began to take place. Shortly after 2338 UTC, ΔV_{max} in mesocyclone 3 had increased to greater than $60\,m\,s^{-1}$, and of similar intensity to that

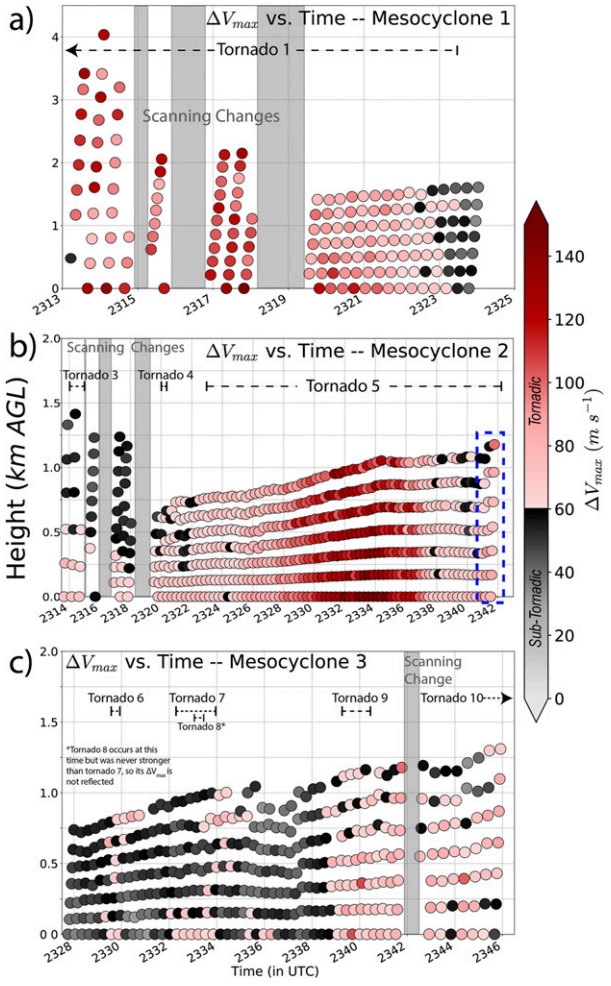

FIG. 7. The $\Delta V_{\max}$ as a function of time and height for three mesocyclone cycles (a) 1, (b) 2, and (c) 3 observed by RaXPol. The times at which data were missing because of radar scanning strategy changes or breaks in data collection are indicated with gray shading. In (b), the effects of the Fujiwara interaction between tornadoes 5 and 9 are indicated by the blue-outlined box. In this case, it was found that a $\Delta V_{\max} > 60\,\mathrm{m\,s^{-1}}$ in RaXPol data corresponded most closely with visual observations of tornado formation and the damage based on an aerial survey. Thus, in this case, $\Delta V_{\max} > 60\,\mathrm{m\,s^{-1}}$ is colored in shades of red, indicating when the vortex became tornadic. The tornadoes corresponding to each mesocyclone and their time spans are indicated in each panel. While tornado 8 was observed by RaXPol, it occurred in mesocyclone 3 simultaneously with tornado 7 but was never at any point in time stronger than tornado 7. Thus, its time span is indicated, but its intensity is not reflected in the plot.

observed in mesocyclone 2 as it was weakening. Over the next several minutes, mesocyclone 3 began to absorb mesocyclone 2 in a Fujiwara-like manner (Fujiwara 1943), eventually merging both areas of rotation into one. Figures 5d and 5e illustrate this process from a single-Doppler perspective as the two areas of rotation merged. As the two regions of rotation approached one another, mesocyclone 2 moved relatively quickly and well to the northeast of its original track. Meanwhile, mesocyclone 3 became quasi stationary over a short period of time. This can also be observed, albeit indirectly, in Fig. 7, in which the heights of the vortex centers observed at each elevation exhibit a "jump" in observed altitude, which can be inferred to be a result of a sudden increase in distance from RaXPol and thus a relatively quick increase in observed vortex height. Similarly, a decrease in vortex height associated with mesocyclone 3 suggests that the vortex's forward motion briefly ceased and perhaps backed up toward the location of the radar for a brief period of time.

As the mesocyclone merger was ongoing, mesocyclone 3 produced another tornado, this one the ninth of the day. Tornado 9 began shortly after 2339 UTC and lasted approximately 90–120 s (Fig. 5). Unlike the other five short-lived tornadoes observed by RaXPol on this day, tornado 9 initially appeared as if it would become the third major tornado. Figure 4 shows the short track of tornado 9, which also exhibited a ribbon-like path likely due to orbiting of the parent mesocyclone as it translated across the surface. Figures 5d and 6d show tornado 9 both visually and in single-Doppler data as it moved slowly toward U.S. Route 56. Analysis of $\Delta V_{\max}$ in Fig. 7c shows a maximum intensification near the ground to greater than $100\,\mathrm{m\,s^{-1}}$, but only for a short time. Contrary to the previous short-lived tornadoes, tornado 9 occurred under a mesocyclone that had reached tornado strength throughout the observed column, yet failed to persist for any substantial length of time. We speculate that the brevity of tornado 9, despite its brief period of high intensity, was likely a result of interactions with the dying mesocyclone 2. A momentum surge evident to the south and east of tornado 5 was responsible for the quick demise of tornado 5, but also likely played a role in dissipating tornado 9 as the mesocyclones became increasing close together as a result of the Fujiwhara interaction.

Despite initial attempts to produce a long-lived tornado, mesocyclone 3 continued northward over the next several minutes. At 2346 UTC, RaXPol relocated 4 miles northward of the original location, but remained on U.S. Route 283 south of Dodge City. Unfortunately, heavy traffic and hail greater than 3 in. (~7.5 cm) in diameter falling across U.S. Route 283 prevented prompt relocation of the radar and observation of the genesis of tornado 10. By the time RaXPol was redeployed at 2356 UTC, a multiple-vortex tornado 10 was already well under way on the west side of Dodge City (Fig. 6e). Because of our inability to obtain a closer deployment location quickly, RaXPol settled on deploying over 20 km from the tornado and thus collected mostly single-elevation (1.5°) data on the tornado (Fig. 5e).

RaXPol observed 9 of the first 10 tornadoes produced by the Dodge City storm until operational logistics made closely following the storm too difficult to continue. Following RaXPol deployment 2, three more tornadoes were produced by a fourth mesocyclone, one of which was observed and photographed from RaXPol as it was in transit on the northeast side of Dodge City.

5. Low-level debris signature evolution

Previous studies have examined the debris-signature characteristics in tornadoes, especially more recently as additional radars with the capability to collect high spatiotemporal

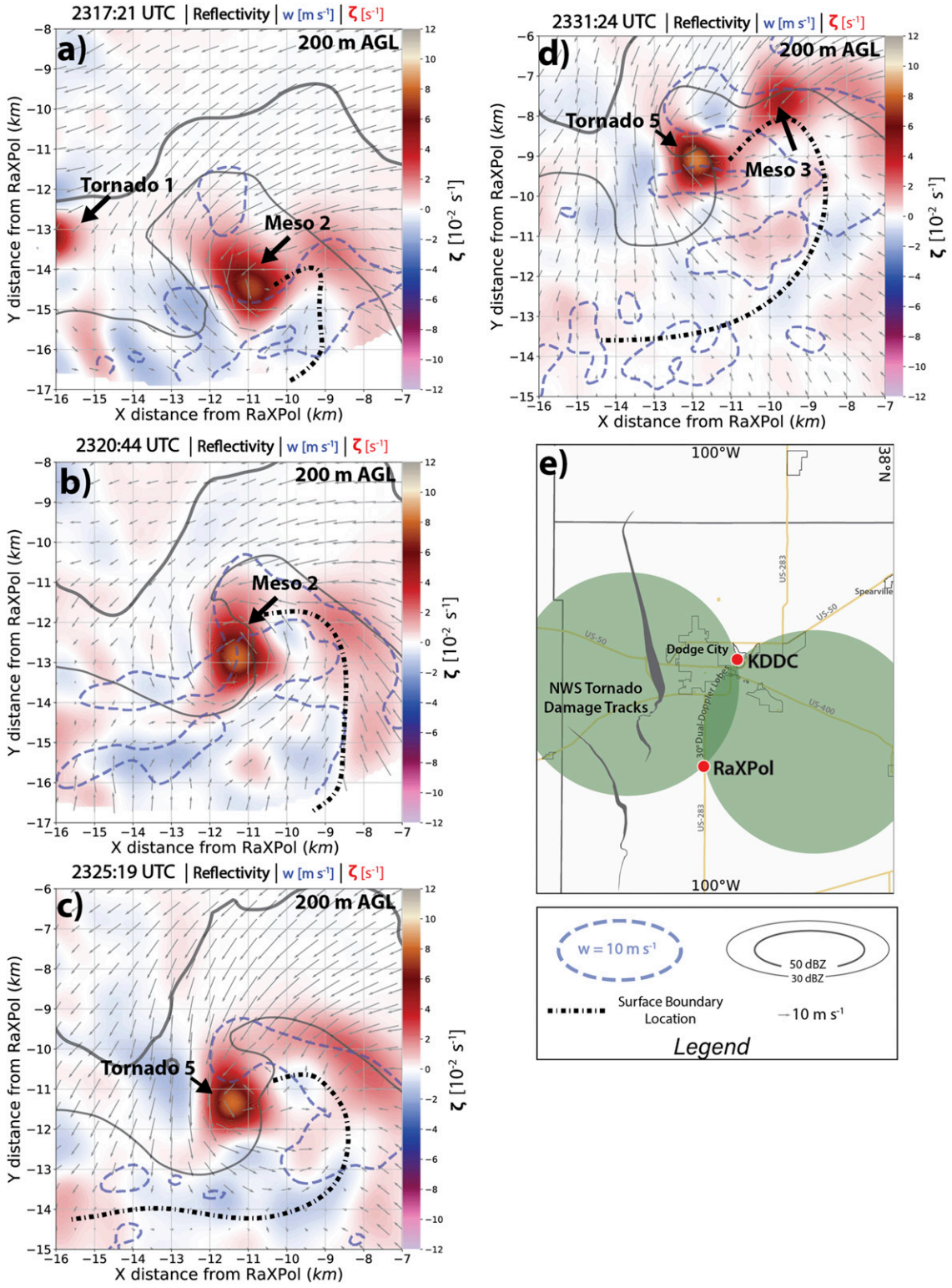

FIG. 8. Dual-Doppler analyses between RaXPol and KDDC, produced using a method that is consistent with Wienhoff et al. (2018), for (a) 2317:21, (b) 2320:44, (c) 2325:19, and (d) 2331:24 UTC. In (a)–(d), vertical velocities greater than 10 m s^{-1} are indicated with a dashed blue line, and radar reflectivities greater than 30 and 50 dBZ are indicated as well. Vertical vorticity values at each time are color contoured. The location of the surface boundary in (a)–(d) is indicated with a dot–dashed black line. (e) The locations of both RaXPol and KDDC, the 30° dual-Doppler lobes, and the NWS damage tracks corresponding to the analyses in (a)–(d).

resolution data have come into existence (e.g., Griffin et al. 2019; Houser et al. 2016; Mahre et al. 2018; Snyder and Bluestein 2014; Wakimoto et al. 2018). However, the majority of the data presented herein (RaXPol D1) were collected during a long, largely uninterrupted, deployment with the majority of volume scans shallow, and minimal beam blockage to interfere with near-surface observations. For these reasons, this case offers a unique opportunity to examine the TDS near the ground, as it evolves with respect to changes in the intensity of the tornadoes, and with respect to changes in ground cover.

Debris signature evolution

Although nine different tornadoes were observed in this case, the evolution of the TDS in tornadoes 1 and 5 are examined herein since each was the dominant tornado associated with mesocyclones 1 and 2, respectively. For each, the area of the debris signature was estimated at 0° elevation for each volume using debris-signature criteria of $\rho_{hv} < 0.80$, and reflectivity > 20 dBZ, which are similar to those used in previous studies but tailored to best suit this case (Griffin et al. 2017, 2020; Ryzhkov et al. 2005; Schultz et al. 2012; Van Den Broeke 2015).[5] Sensitivity of the debris signature area to changes in the selected signature criteria were assessed by iteratively reducing the reflectivity and ρ_{hv} thresholds until further changes resulted in minimal additional effects to the TDS size, and then manual tracking of debris was used to ensure that all relevant regions of debris had been included. At the selected values, small perturbations in TDS criteria result in minimal changes in the calculated TDS, but emphasis in this case will be placed on *relative* changes in the debris signature size, and *not* the specific area of the TDS. To be considered part of the TDS, segments must be connected to or fall no more than 1 km away from the primary TDS (i.e., that which is collocated with the tornado vortex signature).

1) TORNADO 1

Evolution of the TDS over an ~4-min period is examined in Fig. 9. Initially, a relatively strong tornado was observed with a $\Delta V_{max} > 132.5\,m\,s^{-1}$ (Fig. 9b), as well as a circular ρ_{hv} "hole" and "weak echo hole" in reflectivity (Figs. 9a,c). Several minutes later, the debris signature developed a comma-shaped structure with an elongated appendage on the southern side of the tornado vortex signature (TVS), similar to the findings of Bodine et al. (2014) and Houser et al. (2016). Although the tornado was weakening through this time period (2317–2321 UTC), the area of the TDS nearly tripled and had an east–west-oriented appendage, which later became more north-south oriented as it progressed from the tornado's west and southwest side around to the south and east side. This episode of debris shedding, more formally known as a debris ejection, was first described by Kurdzo et al. (2015) in the Moore, Oklahoma (2013), tornado in relation to storm-scale momentum surges, and later by Houser et al. (2016) in the El Reno (2011) tornado. Although it remained largely invisible to RaXPol due to its flow-perpendicular viewing angle, more thorough analysis of the available dual-Doppler and KDDC data revealed the presence of an RFD surge on the southwest side of the tornado originating at ~2317 UTC. Radial divergence (indicated by the blue dashed lines in Figs. 10a,c,d) from KDDC in this region shows the progression of RFD outflow (Figs. 10c,d) away from the mesocyclone and moving southeastward with respect to the tornado, albeit relatively subtle given the only marginally better viewing angle of KDDC. However, the dual-Doppler analysis during this time period shows a much more prominent RFD surge at 2317:21 UTC. Figure 10b shows the dual-Doppler divergence field (color contoured) with vertical vorticity overlaid (gray dashed contours), clearly illustrating the southward directed surge emanating from the storm west of the tornado, and a clear convergence line as result (Fig. 10b, black dashed line).

Direct examination of the TDS from tornado 1 reveals several notable characteristics as tornado 1 weakened. First, growth of the TDS was the most substantial during the demise of tornado 1. The tornado's ΔV_{max} (Fig. 11a) weakened at 0° from $> 140\,m\,s^{-1}$ to subtornado strength by 2324, during which time the TDS grew to $\sim 6\,km^2$ and maintained this size throughout the remainder of the tornado's life. Given the presence of the RFD surge shown in Fig. 10 and the growth of the TDS shown in Figs. 9 and 11, it is likely that this RFD surge (or occlusion downdraft in this case) was responsible for the debris ejection observed at 0°, 3°, and 6° elevation, and the subsequent occlusion of the tornado responsible for rapid weakening. Additionally, in the absence of a tornado, growth of the debris signature can occur as a result of debris fallout (e.g., Bluestein et al. 2018; Bodine et al. 2014; Houser et al. 2016). To the authors' knowledge, this is the first time that this has been documented with a radar with a sampling rate adequate for capturing tornado evolution. In addition, 90th-percentile reflectivity and 10th-percentile ρ_{hv},[6] consistent with suggestions from Bodine et al. (2014), were examined as the tornado decayed. Both ρ_{hv} and reflectivity remained approximately constant while the tornado was in progress. As the tornado weakened and dissipated, reflectivity decreased and ρ_{hv} increased slightly, as expected. However, the TDS area at 3° and 6° increased, while the TDS area at 0° dropped slightly. Examination of RaXPol data post tornado 1 (not shown) and Fig. 11d suggests that this upward trend aloft is likely the result of some debris fallout near the location of the dissipated tornado. We speculate that the downward trend in TDS area at 0° post tornado is

[5] Selected TDS criteria were initially chosen on the basis of recommendations of previous studies and then were adjusted through testing of range of ρ_{hv} and reflectivity for several select TDSs. Values were adjusted to the optimal level that most often correctly outlined regions of debris for this case. Although these values will likely give similar results in any case, the authors recommend that values be carefully adjusted for any additional case studies.

[6] The 90th-percentile reflectivity and 10th-percentile ρ_{hv} were adapted as a more robust method of measuring these parameters by avoiding the statistical noise associated with simply using maximum/minimum values, and with little change in the resulting values (D. Bodine 2020, personal communication).

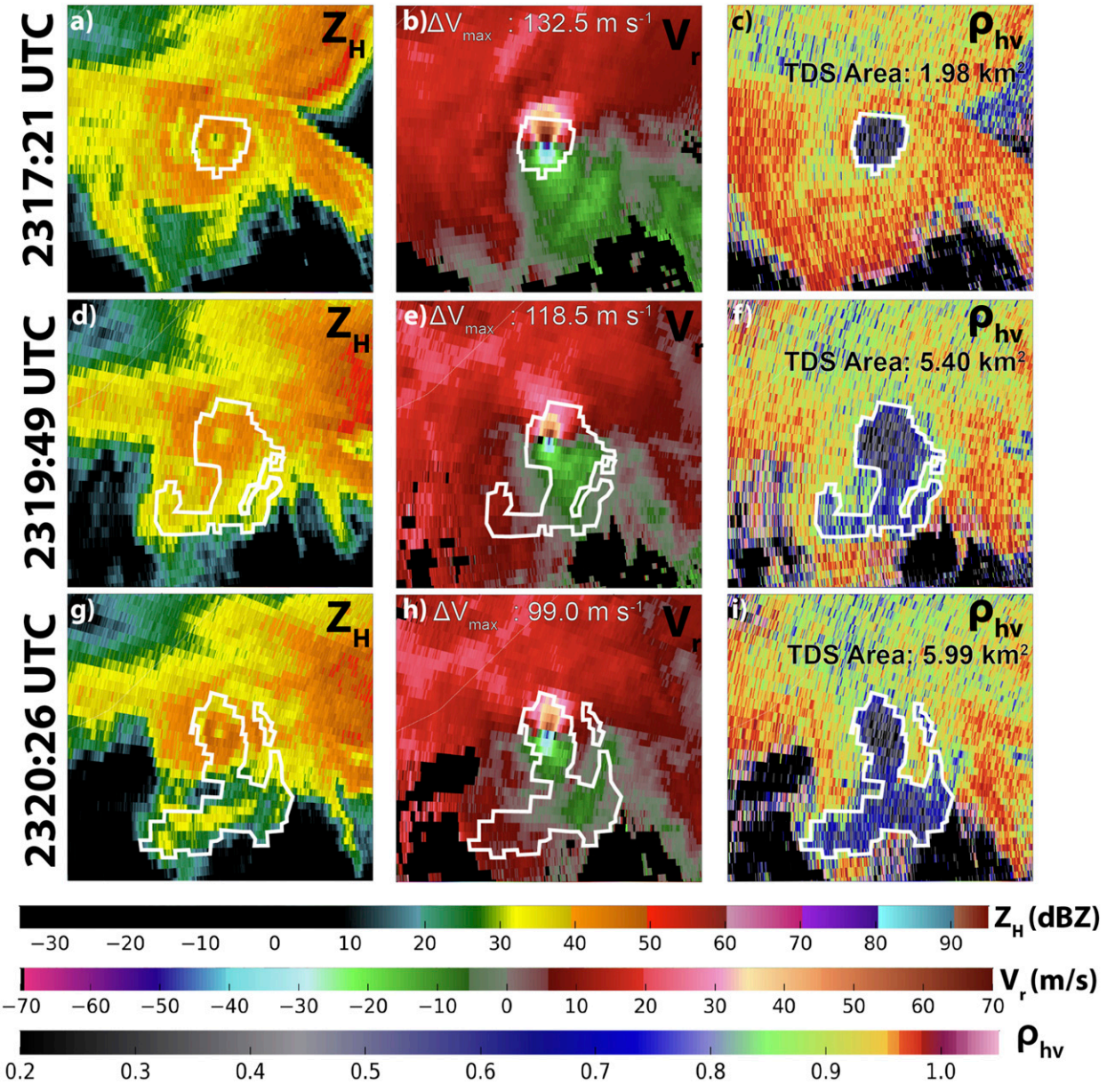

FIG. 9. RaXPol (left) radar reflectivity, (center) radial velocity, and (right) cross-correlation coefficient are shown at (a)–(c) 2317:21, (d)–(f) 2319:49, and (g)–(i) 2320:26 UTC during tornado 1. For each time, the white-outlined area highlights the approximate location of the TDS, and the TDS area and ΔV_{max} are indicated for each time.

simply a result of more debris very near the surface falling to the ground than that falling into this region of the radar beam from above, resulting in a small net decrease in TDS area at 0°. Changes in the polarimetric variables will be specifically examined with respect to the surface cover type in the next section.

2) TORNADO 5

The entire life cycle of tornado 5 was observed by RaXPol, providing a clearer depiction of the polarimetric variable evolution from genesis through dissipation. Initially, tornado 5's ΔV_{max} remained quasi-steady and, despite peaking between 70 and 80 m s^{-1}, no tornado was observed (Fig. 12a). Just before 2325 UTC, a marked increase in ΔV_{max} was noted as the tornado track began. As the tornado strengthened to its peak intensity over an 8–10-min period, observed 90th-percentile radar reflectivity and 10th-percentile cross-correlation coefficient follow our generally expected trends (Figs. 12b and 12c, respectively); that is, reflectivity remained relatively constant, on average, throughout. Conversely, ρ_{hv} began steadily falling after 2327 UTC, as did 10th-percentile Z_{DR} (Fig. 12e). As mentioned earlier, only the trends in the TDS

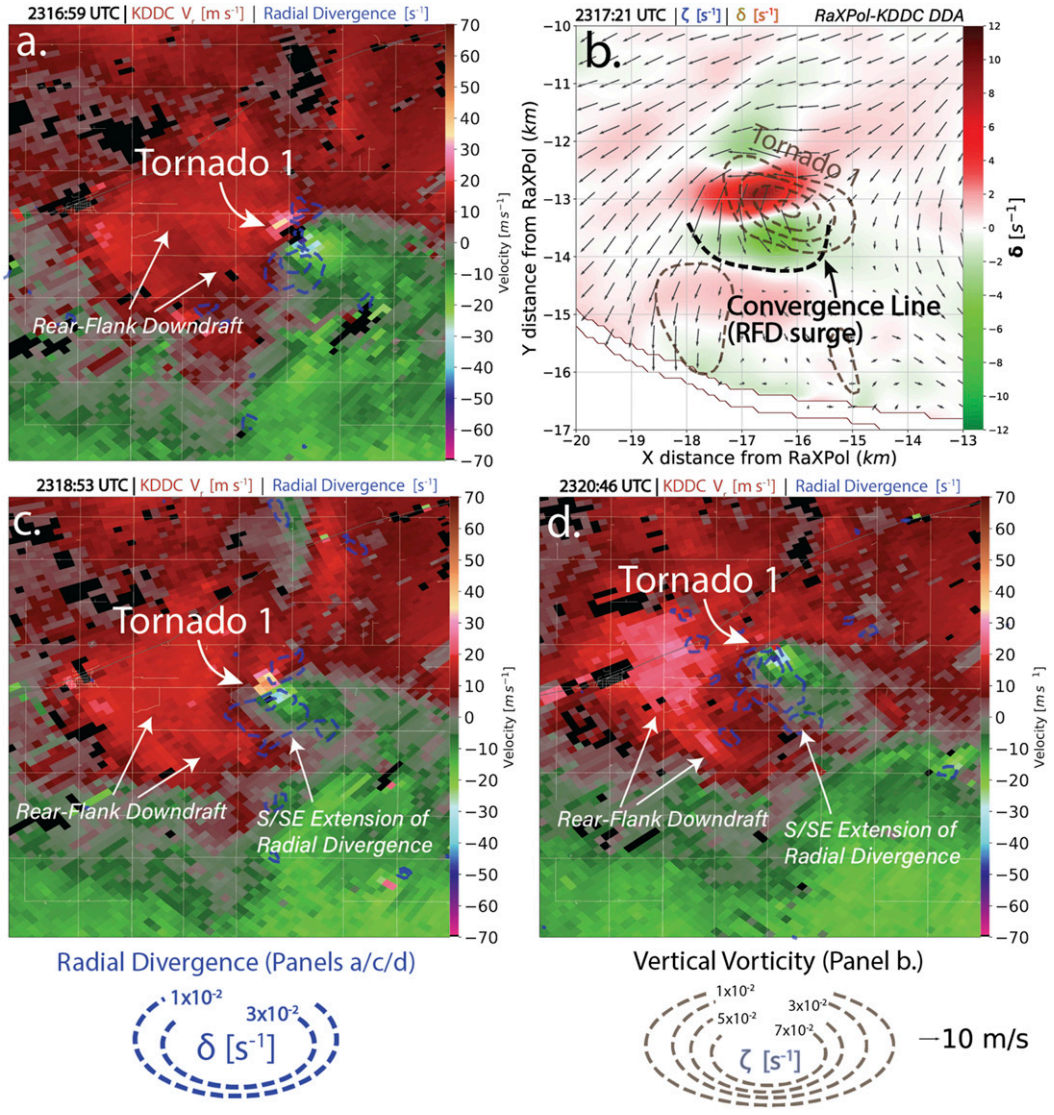

FIG. 10. (a),(c),(d) Single- (KDDC) and (b) dual-Doppler analysis (DDA) of tornado 1 during the time period spanning from ~2317 to 2321 UTC. During this time, tornado 1 underwent a significant debris ejection and subsequent weakening of the tornado shortly thereafter. In (a), (c), and (d), regions of radial divergence are circled by blue dashed lines. A DDA similar to that shown in Fig. 8, but farther west, is shown in (b). Color contoured in (b) is divergence obtained from the dual-Doppler, and positive vertical vorticity is contoured in the dark-gray dashed line.

area are considered, since the exact values were observed to fluctuate on a sweep-by-sweep basis and can include regions of non-debris-related signal. For example, the initial values > 0 (~2323: 30 UTC) are likely associated with a developing weak echo hole, which possessed relatively low ρ_{hv} owing to the centrifuging of hydrometeors, reflectivity just above the minimum 20-dBZ threshold, and $\Delta V_{max} > 60\,m\,s^{-1}$, satisfying our debris signature criteria.

Despite the significant downward trend in ρ_{hv} as ΔV_{max} increased, the area of the tornado debris signature remained relatively steady on average with minimal increase through 2333 UTC. After 2333, the TDS area began to increase significantly as the tornado dissipated, similar to the findings of Bodine et al. (2014) and Houser et al. (2016). Meanwhile, both ρ_{hv} and Z_{DR} had reached their minima and had begun to increase despite continued growth of the debris signature. Although we expect some relationship to exist between ΔV_{max}, ρ_{hv}, Z_{DR}, and TDS area, it is obvious from this analysis that these parameters are likely, at times, modulated by other factors. These potential factors are discussed in the next section.

6. Discussion

Although it is reasonable to expect that tornado intensity is primarily responsible for the modulation of TDS size and characteristics, analysis of the observations collected by RaXPol during

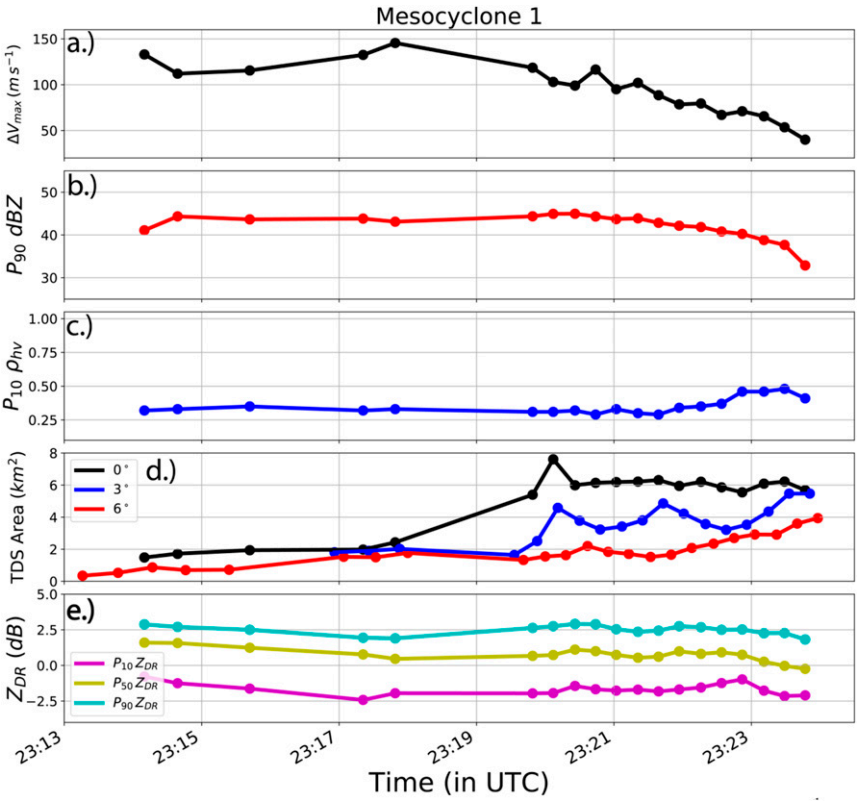

FIG. 11. Time series plots of (a) $\Delta V_{\max}$ ($\mathrm{m\,s^{-1}}$); (b) 90th-percentile radar reflectivity (dBZ); (c) 10th-percentile cross-correlation coefficient; (d) TDS area at 0°, 3°, and 6° elevation ($\mathrm{km^2}$); and (e) 10th-, 50th-, and 90th-percentile Z_{DR} (dB) obtained from RaXPol data for mesocyclone 1. All time series were obtained from RaXPol data at 0° elevation unless otherwise indicated.

the Dodge City tornadoes provide several examples from which it may be inferred that the primary mechanisms for rapid TDS growth are likely *independent* of changes in $\Delta V_{\max}$. With respect to tornadoes 1 and 5, two particular time periods in which rapid and significant TDS growth occurred (>100% increase in TDS aerial extent), both during the weakening stages of the tornadoes: from 2318 to 2322 UTC in tornado 1, and 2335 to 2339 UTC in tornado 5. During both periods, the TDS growth, which was initially steady and increasing, rapidly increased, yet the vortex was weakening. We speculate that three potential mechanisms may be responsible for these rapid growth periods, aside from explicit changes in vortex intensity: debris ejection and fallout, changes in surface characteristics, and changes in vortex tilt.

a. Debris ejection and fallout

Debris ejections were first observed by Houser (2013) and Houser et al. (2015), described as debris "tails" extending from the primary TDS. Kurdzo et al. (2015) formally defined these tails as "debris ejections," which they described as "an area of debris ejected from the core tornado vortex along a line typically to the south of the tornado…" Kurdzo et al. attributed debris ejections to the occurrence of RFD surges, which intersect the primary TDS and force debris outward in a tail or comma-shaped fashion (Kurdzo et al. 2015; see their Fig. 6). The sharp growth of the TDS area in both tornadoes 1 and 5 is related to debris ejection forced by an RFD surge. In both cases, growth of the TDS generally occurred *slowly* as a result of *increasing* tornado intensity, but significant growth in each case coincided with RFD surges, subsequent occlusion, and rapid weakening of the tornadoes in both cases. Figures 13 and 14 concisely illustrate examples in tornado 1 (Fig. 13) and tornado 5 (Fig. 14) of surging momentum around the southern side of the vortex, which is eventually evident on the southeast flank of the tornado. The TDS area is maximized in both cases as a result of the RFD-forced debris ejection and lofting as well as fallout of debris from aloft following the RFD surge.

Although it seems unlikely to result in such massive debris ejections as observed here and in previous cases, we speculate that small, shallow episodes of centrifuged debris can potentially be responsible for debris-ejection-like signatures as a result of periodic destruction and centrifuging of large debris from the tornado. That is, as the tornado destroys a property, relatively large debris (e.g., large limbs, steel/sheet metal, and roofing panels) would be immediately centrifuged away from the center of the vortex leaving smaller debris (e.g., shingles, siding, small limbs, and leaves) to be accelerated into the inflow region at relatively faster speeds than the background flow. This could potentially result is enhanced radar-observed radial velocities, and sawtooth-like protrusions from the circular TDS extending outward in a similar fashion to a debris

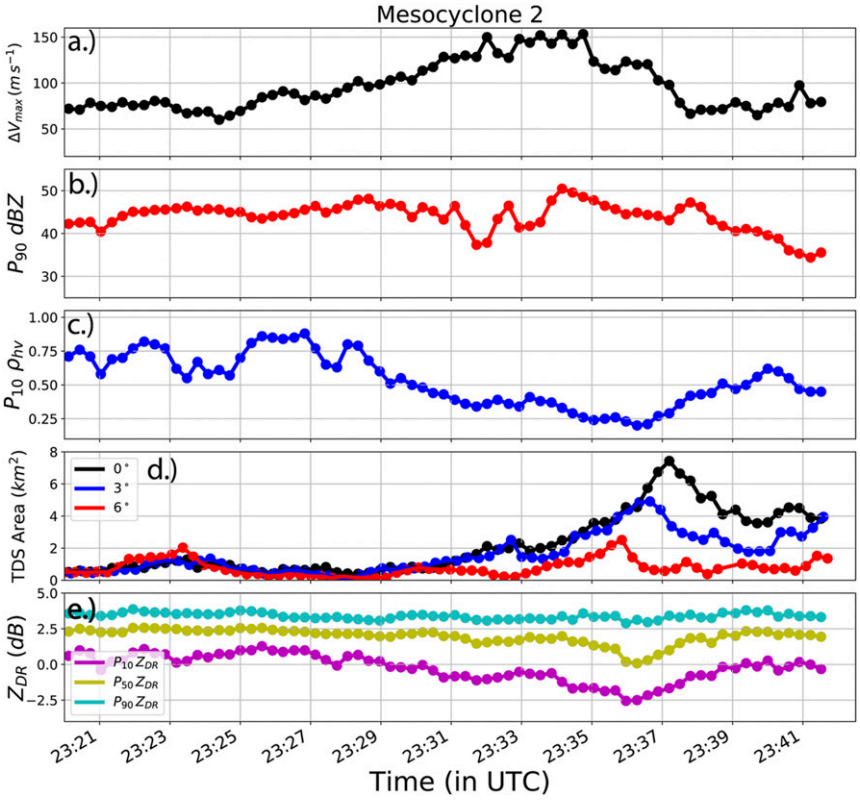

FIG. 12. As in Fig. 11, but for mesocyclone 2.

ejection, but on a much smaller scale. We hope that this may serve as a potential focus for future tornado-debris-related studies.

b. *Surface characteristics*

In contrast to debris ejections, another potential link to TDS growth is via changes in the near-surface characteristics. Especially in rural areas where man-made structures are relatively sparse, tornado debris is largely composed of that which covers the surface, which in this case varies between dirt/sand, grass, and crops (e.g., wheat). As a tornado moves between fields with different surface cover characteristics, for example from an unplowed field with a residual root system, to a plowed, terraced dirt field with an excess of loose soil that can easily be lofted, the amount of accumulated tornado debris can vary substantially (Van Den Broeke and Jauernic 2014). In this case, the high spatiotemporal resolution of this dataset allows for the comparison of the polarimetric variables in each scan to the ground cover in each case.

Figures 15 and 16 compare several radar variables, including $\Delta V_{\max}$, ρ_{hv}, and radar reflectivity in the tornado, with the land cover over which the tornado traversed. The terrain cover was added to the analyses via aerial photography, taken several days after the event. See Wakimoto et al. (2018) for more on the aerial damage survey and photogrammetric analysis of the event.

As tornado 1 moved to the northwest (Fig. 15), little change in the polarimetric signatures were observed as the tornado weakened, although $\rho_{\text{hv}}$was smallest during the period in which the TDS area was the greatest (Fig. 11). The tornado resided over mostly dirt fields during this time. As the tornado encountered the farmstead, a brief reduction in $\Delta V_{\max}$ was observed potentially as a result of tornado debris loading (e.g., Bodine et al. 2016; Lewellen et al. 2008), but little change in the polarimetric signatures was observed (Figs. 17a,b). As the tornado dissipated and crossed U.S. Route 56 just before 2323 UTC, there were notable decreases in Z_{DR} as the tornado moved through a small grass field and two larger wheat fields (Figs. 15 and 17). A similar decrease was also observed in ρ_{hv}. We speculate that as the tornado moved into the wheat/grass, despite the tornado being weak and near dissipation, the tornado was still able to loft wheat heads/stems and blades of grass, both of which could potentially cause a reduction of Z_{DR} and ρ_{hv} if oriented vertically, as discussed in Umeyama et al. (2018) and Wakimoto et al. (2018). Another possibility is that debris fallout at the end of tornado 1, as previously discussed (Fig. 11d), could have contained large amounts of grass and wheat stems from previous portions of the track especially given that these debris types are easily lofted by a tornado.

For tornado 5, several points along the track also exhibited changes potentially related to the ground cover (Figs. 16 and 17). Just after 2327 UTC, a brief, sharp decrease in ρ_{hv} and a small spike in TDS area (Fig. 12) were noted as the tornado was situated over a terraced dirt field (Figs. 16 and 17). Shortly thereafter, as the tornado began moving through several large

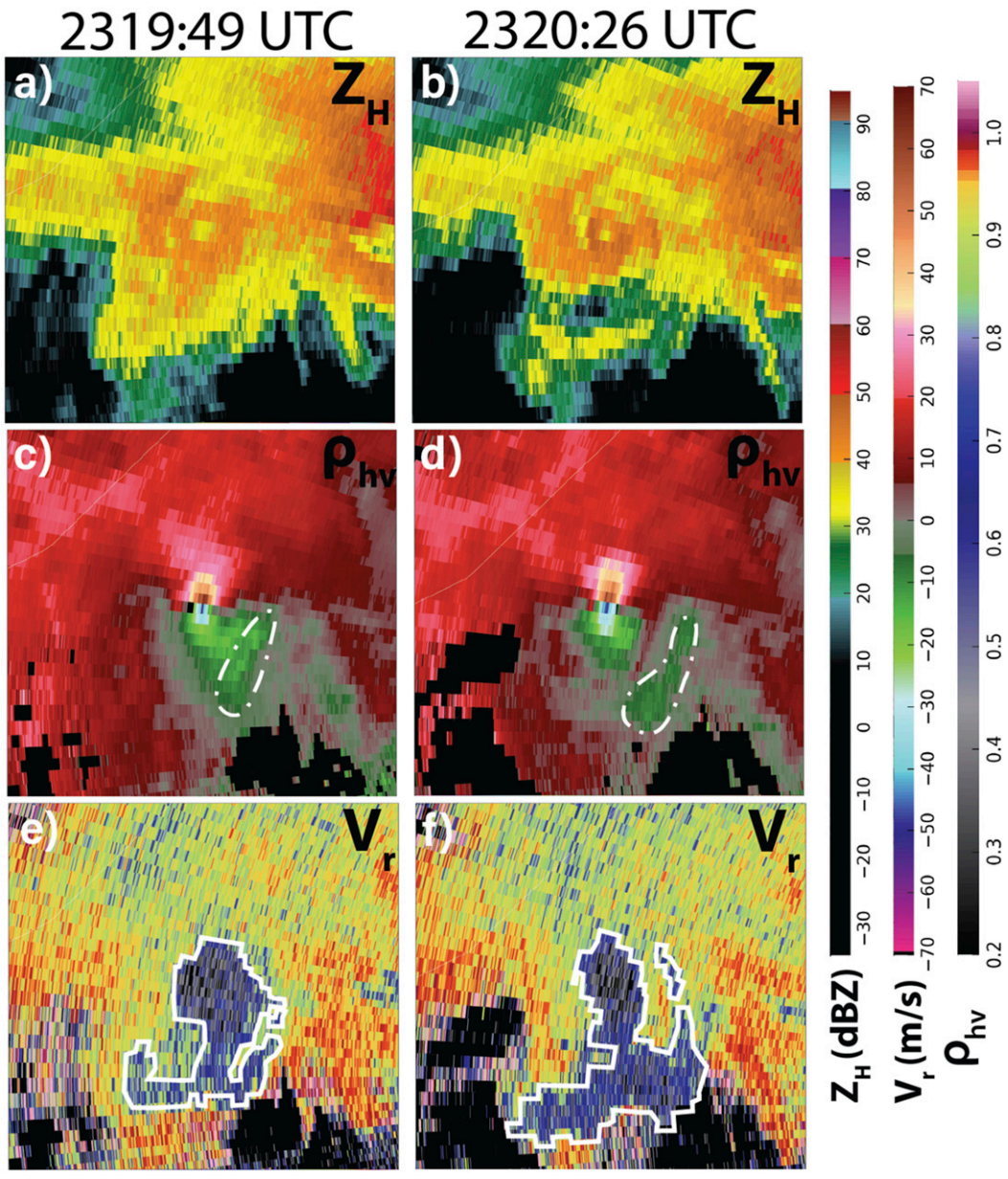

FIG. 13. RaXPol (a),(b) radar reflectivity; (c),(d), radial velocity; and(e),(f) cross-correlation coefficient at (left) 2319:49 and (right) 2320:26 UTC during tornado 1. The dot–dashed white lines in (c) and (d) indicate the location of a momentum surge, which was associated with the debris ejection from tornado 1. The solid white lines in (e) and (f) illustrate the growth of the TDS as the momentum surge, which was not initially evident in RaXPol radial velocities because of the radar's viewing angle, moved eastward around the southern side of tornado 1. Each panel is approximately 6 km by 6 km.

wheat fields, Z_{DR} decreased as expected, becoming steadily more negative throughout as the tornado both strengthened and more wheat was presumably lofted by the tornado. The progression through each of the field types is specifically outlined in Fig. 17c. Once the tornado moved out of the wheat field, Z_{DR} stabilized briefly, but ρ_{hv} began a rapid drop to ~0.2 as it moved out over a dirt field, and eventually over a second terraced dirt field. The tornado's residence over the terraced field at ~2334 UTC corresponds to the beginning of the rapid growth of the TDS area (Fig. 12). While it is most likely that the RFD-surge-induced debris ejection was the primary reason for TDS expansion at this time, significant ground scouring was observed as well as discussed in Wakimoto et al. (2018); it occurred in a terraced field. With an uptick in TDS area and sharp reduction in ρ_{hv} observed to occur in several different terraced fields, we

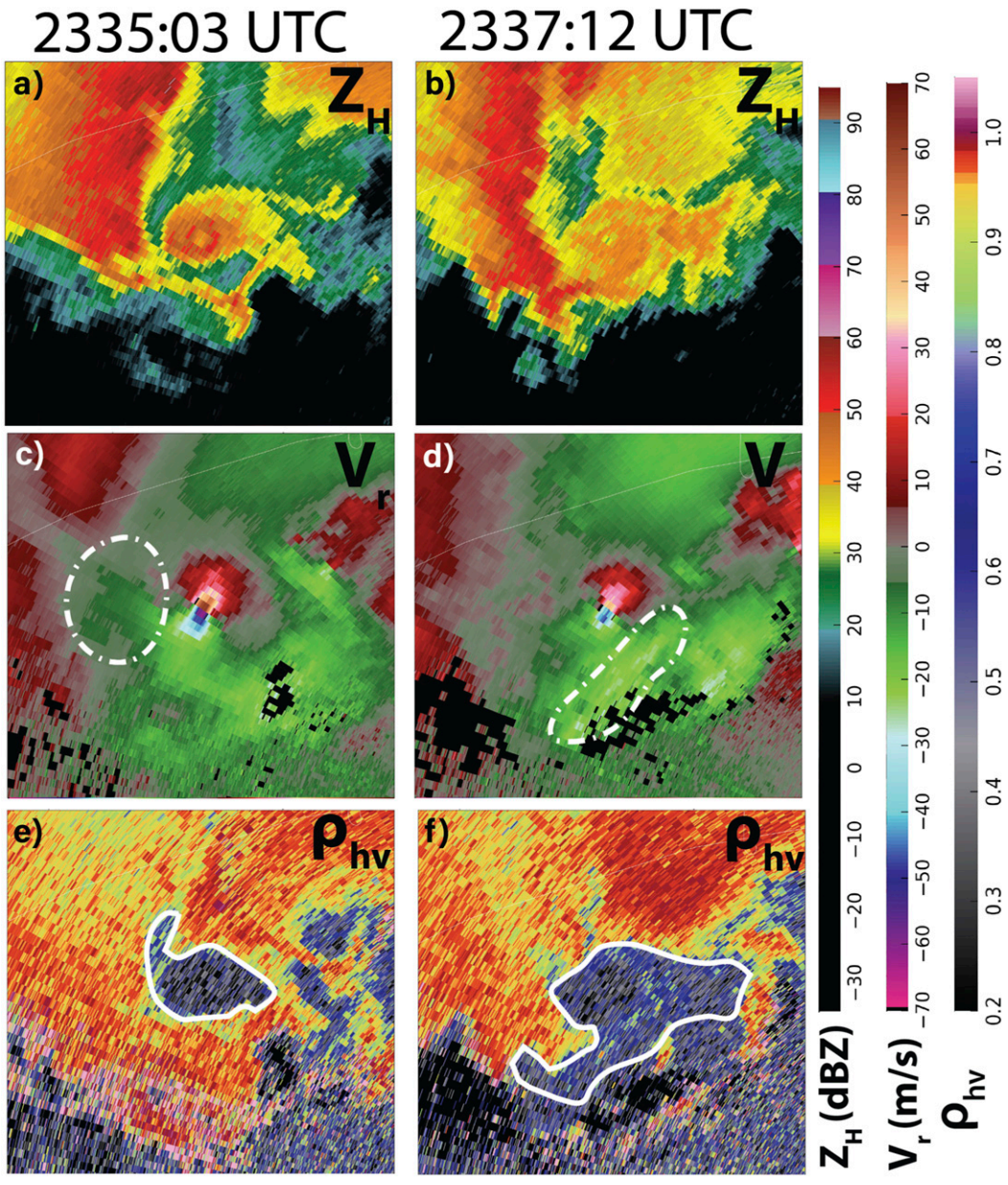

FIG. 14. RaXPol (a),(b) radar reflectivity; (c),(d), radial velocity; and(e),(f) cross-correlation coefficient at (left) 2335:03 and (right) 2337:12 UTC during tornado 5. In (c) and (d), the dot–dashed white line highlights the initial RFD surge, which moved eastward around the south side of the tornado. The solid white lines in (e) and (f) shows the movement and growth of the TDS, which also illustrates the east and southeast motion of the RFD surge around the vortex, resulting in a debris ejection from tornado 5. Each panel is approximately 6 km by 6 km.

speculate that the terracing is perhaps playing a role in the additional debris production in two potential ways: 1) terracing, a soil conservation technique aimed at preventing erosion caused by surface runoff, means that an unplanted, recently plowed field with loose soil would be especially susceptible to soil scouring, and 2) terracing could induce channeling of the near-surface wind field, causing it to become even more intense and leading to surface scouring. Although difficult to prove which was responsible for the observed scouring, it seems plausible that terracing is also partly responsible for the rapid growth of the TDS observed during tornado 5.

c. Vortex tilt

A third factor that is potentially responsible for TDS growth is the tilt of the tornado vortex. Numerous studies have

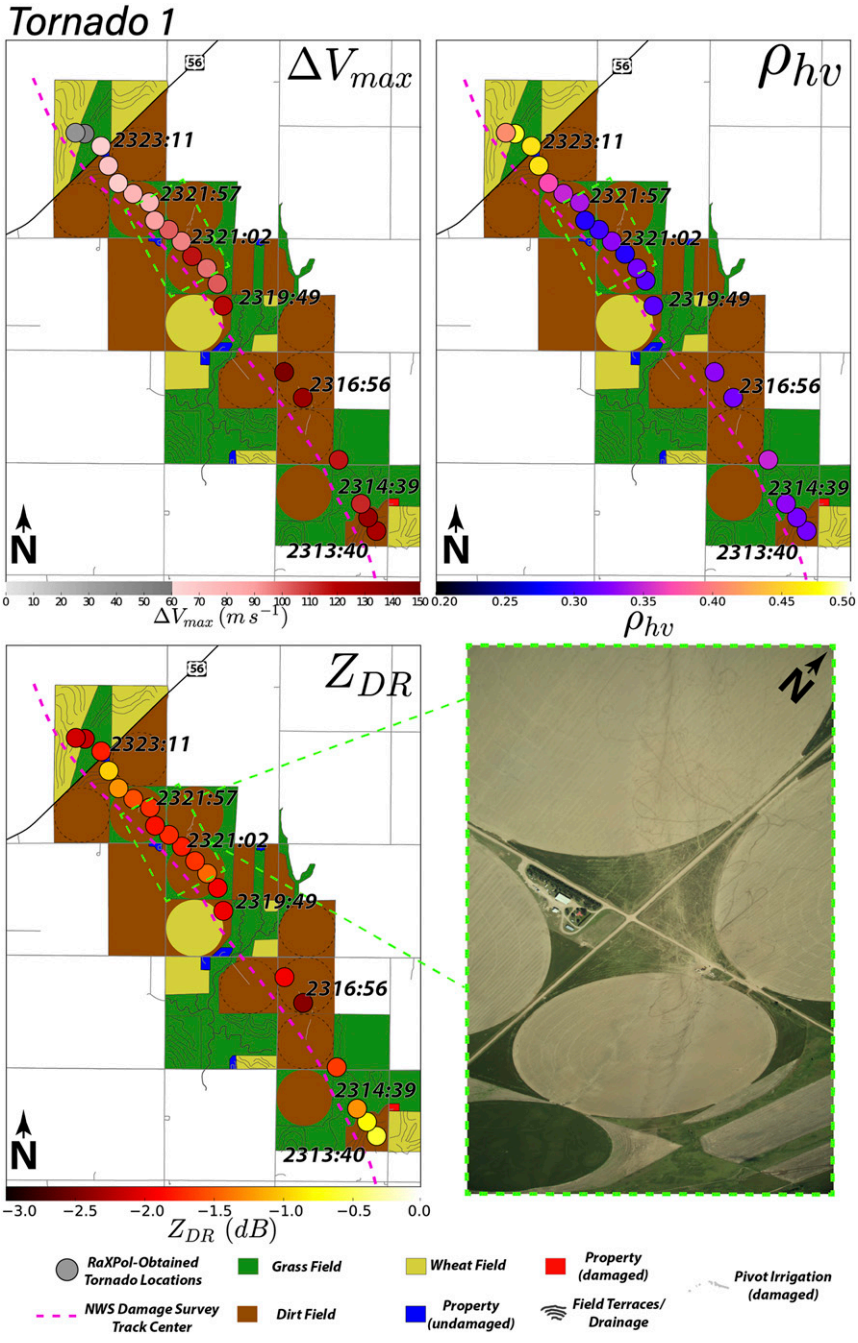

FIG. 15. Comparisons of (top left) $\Delta V_{\max}$, (top right) ρ_{hv}, and (bottom left) Z_{DR} with ground-cover characteristics obtained from aerial photography of tornado 1's damage path. (bottom right) Photograph of the rectangle in (a)–(c) that is outlined in light green, showing the abrupt change in tornado 1's path as it destroyed a small farmstead. In (a)–(c), the small circles represent the location of the tornado obtained from RaXPol data, and each is colored on the basis of the corresponding color bar for each panel. The indicated land covers include grass fields, wheat fields, dirt fields, terraced fields (for each of the three field types), damaged and undamaged farms, and damaged pivot irrigators for all parts of the track with which the tornado came into direct contact. In (a)–(c), the magenta dashed line represents the NWS-surveyed tornado center, for reference.

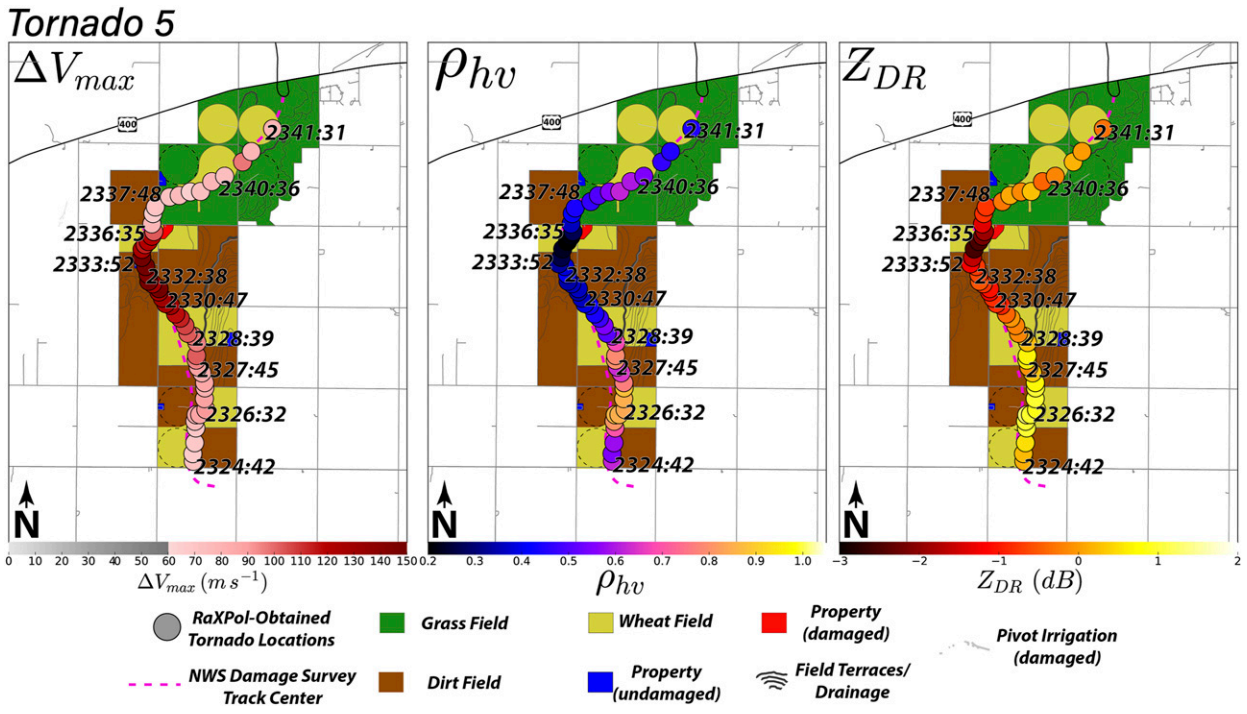

FIG. 16. As in Fig. 15, but for the track of tornado 5.

noted the presence of a highly tilted vortex, especially during genesis/dissipation phases (e.g., Bluestein 2013; Bluestein et al. 2019, 2007; French et al. 2014). From this case, it is proposed that a tilted vortex (i.e., greater displacement between the RaXPol-observed near-surface (0° elevation) and midlevel (6° elevation) vortex locations) aided in additional lofting of debris as compared to a completely vertically erect tornado.

If we consider a tornado that is completely perpendicular to the surface, the swirling component of the wind field around the tornado is parallel to the surface, leaving the potential *lofting* of tornado debris to only the vertical component. For a tilted tornado, the swirling component is no longer parallel to the surface and thus has some component of the wind in the *vertical* direction. In this particular case, as the tornado tilted northward under the northward translating updraft, an enhanced wind component in the vertical would support more substantial growth of the TDS in the western/southern quadrants. Conversely, the eastern and northern quadrants experience more downward-directed velocities around the vortex, forcing accumulated debris toward the surface. We assume that the vortex is oriented normal to the surface near the surface but begins to tilt just above the ground. This idea is in support of observations made by previous studies of southward-extending debris tails, although those studies primarily discussed the presence of comma-shaped debris signatures being related to RFD-surge induced ejections (e.g., Houser et al. 2015; Kurdzo et al. 2017).

For tornado 5, oscillations in tilt about the surface-level rotation center [i.e., if we consider the surface-level rotation center (0° elevation) to be stationary with respect to the midlevel rotation center (6° elevation)] occurred with a periodicity of ~4 min prior to tornadogenesis, after which the tilt stabilized (~25°; Fig. 18d). The tilt then decreased as the tornado approached maturity/peak intensity, followed by substantial tilting to the north and northeast as weakening began. Similar observations from maturity through dissipation were observed for tornado 1, although data collection on tornado 1 began only shortly before its most intense period (Figs. 18a,c).

Despite the intriguing tilt-related behaviors observed in these cases, we focus only on the period after peak intensity when the vortex tilt increased most substantially. In both cases, as the tornado began to take on additional tilt, the TDS areas grew. Especially in the case of tornado 5, limited, but steady, growth of the TDS occurred from 2328 to 2334 UTC (Fig. 12), during the period in which the tornado maintained constant tilt. The most dramatic tilting of the vortex began at ~2335 UTC, coinciding with the beginning of the most rapid growth stage of the TDS.

The southward extension of the TDS during these periods, but not to the north, supports the hypothesis that vortex tilting may have been responsible for the growth of the TDS southward and eastward as it tilted. However, it is important to address that, especially for cases like tornado 5, the growth of the TDS and the tilt may both be consequences of an RFD surge and subsequent occlusion of the tornado. As the RFD surge occurs, a debris ejection may be the primary cause of TDS growth, and tilting a result of tornado occlusion (Fig. 13), especially since the tornado's influence on TDS growth will decrease with height given the northward tilt of the vortex. While growth of the TDS in tornado 1 may be partially a result of tilting, this case shows that tilting may be a cause or a symptom and requires careful examination to avoid misclassification.

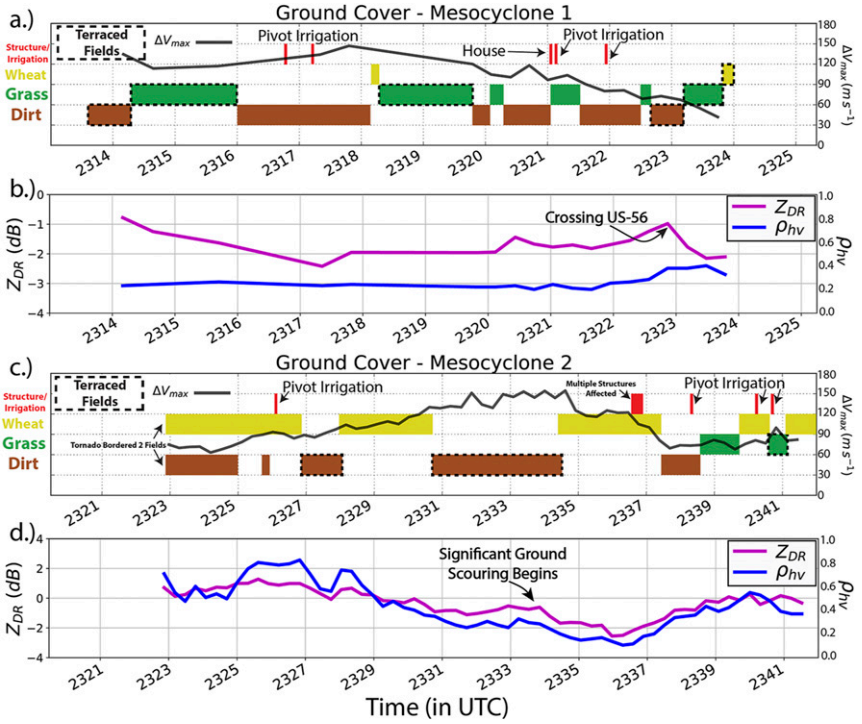

FIG. 17. Land-cover types encountered by tornadoes 1 and 5 and their associated $\Delta V_{\max}$ (black curve), ρ_{hv} (blue curve), and Z_{DR} (purple curve) as a function of time for (a),(b) tornado 1 and (c),(d) tornado 5 as estimated by RaXPol at 0° elevation. In each case, the indicated land-cover type is based on each tornado's location with respect to the specified field types in Figs. 15 and 16. In instances in which two field types are specified, it was impossible to discriminate exactly in which terrain type the tornado was at that particular time as the tornado straddled the divide between two land-cover types. The locations of pivot irrigators and houses/structures are indicated, and all terraced field locations are indicated with a dashed black outline.

7. Summary and conclusions

On 24 May 2016, RaXPol documented one of the most prolific tornado-producing supercells ever recorded by a mobile radar. This case provided the opportunity to examine multiple tornadoes, many of which were observed from genesis through dissipation, with high spatiotemporal resolution and with the benefit of polarimetric radar.

The primary goals of this work were to 1) provide a detailed, tornado-by-tornado analysis of one of the most prolific tornado-producing supercells ever documented by mobile radar and 2) to utilize this unique dataset to examine numerous near-surface tornado debris signatures that occurred as a result of cyclic mesocyclogenesis along a residual outflow boundary (e.g., Adlerman et al. 1999; Burgess 1982). In particular, the factors that are responsible for modulating the size of the TDS were examined with respect to previous studies, and several additional mechanisms for TDS growth were proposed.

In general, tornado strength largely dictates the size of a TDS prior to its decay. That is, a stronger tornado is apt to consume more debris, thus resulting in the expansion of the TDS. However, this study provides several examples where changes in TDS size do not necessarily follow trends in the tornado's $\Delta V_{\max}$, which is a proxy for tornado intensity. RFD surges, which has been previously linked to debris ejections in previous studies (e.g., Kurdzo et al. 2015), was also shown in this case to be the likely cause for the two debris ejections accompanying the tornadoes just prior to occlusion. The near-surface characteristics were also examined via aerial photography and compared to the tornado's location. Both Z_{DR} and ρ_{hv} had responses that were consistent with the underlying surface cover characteristics, especially as the tornado moved through both wheat and terraced dirt fields, although additional work is needed to further isolate the effects of surface cover from other important factors (e.g., tornado intensity). Tornado tilt was also examined as a function of time and compared to the growth and decay of the tornado, which may provide a potential link to the existence of south/eastward extending debris tails, but the rare nature of debris signatures which extend to the north of the primary TDS.

Although it is difficult via observations alone to specify the primary culprit responsible for changes in the TDS, it is shown herein that many, if not all, of these factors could potentially affect changes in the TDS simultaneously. We hope that this case supports the need for additional observational studies of the effects of the underlying surface characteristics on the tornado, including the presence of structures/trees in the

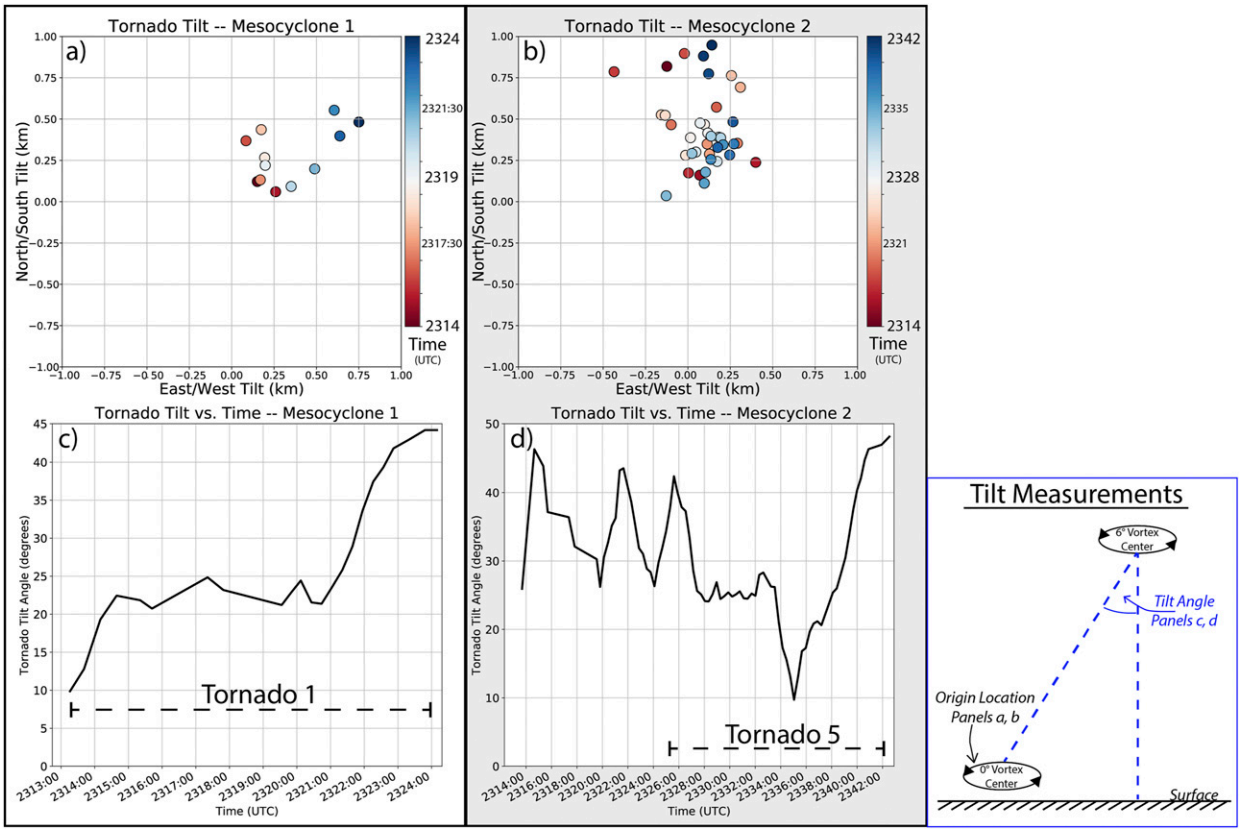

FIG. 18. (a),(b) The X/Y displacement of the midlevel tornado vortex with respect to the location of the surface vortex, and (c),(d) the estimated tilt (in degrees) of the tornado calculated between the vortex location obtained via RaXPol 0° and 6° elevation angles.

path that can be centrifuged away from the tornado, causing changes to a tornado's internal dynamics and impacting additional structures downstream.

Acknowledgments. This work was funded under NSF Grants AGS-1262048 and AGS-1560945. The authors are grateful to Boon Leng Cheong, Danny Feland, John Meier, and Dale Sexton and the Advanced Radar Research Center at the University of Oklahoma for housing and maintaining RaXPol. We thank Kyle Thiem for many fruitful discussions about this work and for his help in reconstructing the tracks of all 13 of the Dodge City tornadoes. Jeff Snyder, David Bodine, Casey Griffin, Trey Greenwood, and Frank Lombardo and the Wind Engineering Lab group at the University of Illinois are also thanked for numerous discussions that helped to strengthen all aspects of this work. The authors are appreciative of the anonymous reviewers whose comments and suggestions significantly improved this study. We also thank Sean Waugh and Sam Dienst for providing useful photographs and videos of the 24 May 2016 event. Under ''Distribution Statement A,'' this work is approved for public release. Distribution is unlimited. James Kurdzo's involvement in this material is supported by the U.S. Air Force under Air Force Contract FA8702-15-D-0001. Any opinions, findings, conclusions, or recommendations expressed in this material are those of the author(s) and do not necessarily reflect the views of the U.S. Air Force.

APPENDIX

Dual-Doppler Analysis Method

In an effort to understand the potential influence of the residual outflow boundary's role in promoting tornadogenesis (Fig. 3e), a dual-Doppler analysis was performed between KDDC and RaXPol to resolve the low-level three-dimensional flow field near the tornado(es). Figure 8e shows the locations of the dual-Doppler baseline between RaXPol and KDDC, which was 13.8 km, and the locations of the 30° lobes.

Radar data were mapped to a Cartesian coordinate system using Observation Processing and Wind Synthesis software (OPAWS; Majcen et al. 2008) and a two-pass Barnes analysis technique (Barnes 1964; Koch et al. 1983). Objective analysis parameters were chosen based on the farthest distance of mesocyclone 2 from KDDC (~17.5 km), which was determined to be the location of interest for the analysis, and are consistent with previous studies (e.g., Kosiba et al. 2013). In this case, a grid spacing of $\delta = 100$ m was used in both the horizontal and vertical, consistent with $\delta = \Delta/2.5$, where Δ is the raw grid spacing of the radar data (Koch et al. 1983). A

horizontal and vertical smoothing parameter of $\kappa = 0.186\,\text{km}^2$ was also used consistent with $\kappa = (1.33\delta)^2$ (Pauley and Wu 1990).

To best mitigate errors in the dual-Doppler analysis associated with substantial differences in radar sampling rate, a spatially variable advection correction technique (Shapiro et al. 2010) was used to temporally interpolate the KDDC data (in a Lagrangian sense) such that they can be paired optimally with the RaXPol analyses given that RaXPol was collecting approximately 15 volumes per one volume from KDDC, which was operating in MESO-SAILS mode (three scans at 0.5° per volume). For more in-depth information on the use of a spatially variable advection correction technique for dual-Doppler analysis, see Wienhoff et al. (2018).

REFERENCES

Adlerman, E. J., K. K. Droegemeier, and R. Davies-Jones, 1999: A numerical simulation of cyclic mesocyclogenesis. *J. Atmos. Sci.*, **56**, 2045–2069, https://doi.org/10.1175/1520-0469(1999)056<2045:ANSOCM>2.0.CO;2.

Alexander, C. R., and J. Wurman, 2005: The 30 May 1998 Spencer, South Dakota, storm. Part I: The structural evolution and environment of the tornadoes. *Mon. Wea. Rev.*, **133**, 72–97, https://doi.org/10.1175/MWR-2855.1.

——, and J. M. Wurman, 2008: Updated mobile radar climatology of supercell tornado structures and dynamics. *24th Conf. on Severe Local Storms*, Savannah, GA, Amer. Meteor. Soc., 19.4, https://ams.confex.com/ams/24SLS/techprogram/paper_141821.htm.

Barnes, S. L., 1964: A technique for maximizing details in numerical weather map analysis. *J. Appl. Meteor. Climatol.*, **3**, 396–409, https://doi.org/10.1175/1520-0450(1964)003<0396:ATFMDI>2.0.CO;2.

Biggerstaff, M. I., and Coauthors, 2005: The Shared Mobile Atmospheric Research and Teaching radar: A collaboration to enhance research and teaching. *Bull. Amer. Meteor. Soc.*, **86**, 1263–1274, https://doi.org/10.1175/BAMS-86-9-1263.

Bluestein, H. B., 2013: *Severe Convective Storms and Tornadoes*. Springer, 456 pp.

——, and A. L. Pazmany, 2000: Observations of tornadoes and other convective phenomena with a mobile, 3-mm wavelength, Doppler radar: The spring 1999 field experiment. *Bull. Amer. Meteor. Soc.*, **81**, 2939–2952, https://doi.org/10.1175/1520-0477(2000)081<2939:OOTAOC>2.3.CO;2.

——, ——, J. C. Galloway, and R. E. McIntosh, 1995: Studies of the substructure of severe convective storms using a mobile 3-mm-wavelength Doppler radar. *Bull. Amer. Meteor.*, **76**, 2155–2170, https://doi.org/10.1175/1520-0477(1995)076<2155:SOTSOS>2.0.CO;2.

——, M. M. French, R. L. Tanamachi, S. Frasier, K. Hardwick, F. Junyent, and A. L. Pazmany, 2007: Close-range observations of tornadoes in supercells made with a dual-polarization, X-band, mobile Doppler radar. *Mon. Wea. Rev.*, **135**, 1522–1543, https://doi.org/10.1175/MWR3349.1.

——, ——, I. PopStefanija, R. T. Bluth, and J. B. Knorr, 2010: A mobile, phased-array Doppler radar for the study of severe convective storms: The MWR-05XP. *Bull. Amer. Meteor. Soc.*, **91**, 579–600, https://doi.org/10.1175/2009BAMS2914.1.

——, K. J. Thiem, J. C. Snyder, and J. B. Houser, 2018: The multiple-vortex structure of the El Reno, Oklahoma, tornado on 31 May 2013. *Mon. Wea. Rev.*, **146**, 2483–2502, https://doi.org/10.1175/MWR-D-18-0073.1.

——, ——, ——, and ——, 2019: Tornadogenesis and early tornado evolution in the El Reno, Oklahoma, supercell on 31 May 2013. *Mon. Wea. Rev.*, **147**, 2045–2066, https://doi.org/10.1175/MWR-D-18-0338.1.

Bodine, D. J., R. D. Palmer, and G. Zhang, 2014: Dual-wavelength polarimetric radar analyses of tornadic debris signatures. *J. Appl. Meteor. Climatol.*, **53**, 242–261, https://doi.org/10.1175/JAMC-D-13-0189.1.

——, T. Maruyama, R. D. Palmer, C. J. Fulton, H. B. Bluestein, and D. C. Lewellen, 2016: Sensitivity of tornado dynamics to soil debris loading. *J. Atmos. Sci.*, **73**, 2783–2801, https://doi.org/10.1175/JAS-D-15-0188.1.

Burgess, D. W., 1982: Mesocyclone evolution statistics. Preprints, *12th Conf. on Severe Local Storms*, San Antonio, TX, Amer. Meteor. Soc., 422–424.

French, M. M., H. B. Bluestein, I. PopStefanija, C. A. Baldi, and R. T. Bluth, 2013: Reexamining the vertical development of tornadic vortex signatures in supercells. *Mon. Wea. Rev.*, **141**, 4576–4601, https://doi.org/10.1175/MWR-D-12-00315.1.

——, ——, ——, ——, and ——, 2014: Mobile, phased-array, Doppler radar observations of tornadoes at X band. *Mon. Wea. Rev.*, **142**, 1010–1036, https://doi.org/10.1175/MWR-D-13-00101.1.

Fujiwara, S., 1943: Report of thunderstorm observation project. Japan Meteorological Agency Rep., 248 pp.

Griffin, C. B., D. J. Bodine, and R. D. Palmer, 2017: Kinematic and polarimetric radar observations of the 10 May 2010, Moore–Choctaw, Oklahoma, tornadic debris signature. *Mon. Wea. Rev.*, **145**, 2723–2741, https://doi.org/10.1175/MWR-D-16-0344.1.

——, ——, J. M. Kurdzo, A. Mahre, and R. D. Palmer, 2019: High-temporal resolution observations of the 27 May 2015 Canadian, Texas, tornado using the atmospheric imaging radar. *Mon. Wea. Rev.*, **147**, 873–891, https://doi.org/10.1175/MWR-D-18-0297.1.

——, ——, and R. Palmer, 2020: Polarimetric radar observations of simultaneous tornadoes on 10 May 2010 near Norman, Oklahoma. *Mon. Wea. Rev.*, **148**, 477–497, https://doi.org/10.1175/MWR-D-19-0156.1.

Houser, J. B., 2013: Observations of supercell tornado evolution using a mobile, rapid-scan, X-band radar. Ph.D. thesis, University of Oklahoma, 264 pp. https://shareok.org/handle/11244/319359.

Houser, J. L., H. B. Bluestein, and J. C. Snyder, 2015: Rapid-scan, polarimetric, Doppler radar observations of tornadogenesis and tornado dissipation in a tornadic supercell: The ''El Reno, Oklahoma'' storm of 24 May 2011. *Mon. Wea. Rev.*, **143**, 2685–2710, https://doi.org/10.1175/MWR-D-14-00253.1.

——, ——, and ——, 2016: A finescale radar examination of the tornadic debris signature and weak-echo reflectivity band associated with a large, violent tornado. *Mon. Wea. Rev.*, **144**, 4101–4130, https://doi.org/10.1175/MWR-D-15-0408.1.

Isom, B., and Coauthors, 2013: The Atmospheric Imaging Radar: Simultaneous volumetric observations using a phased array weather radar. *J. Atmos. Oceanic Technol.*, **30**, 655–675, https://doi.org/10.1175/JTECH-D-12-00063.1.

Koch, S. E., M. desJardins, and P. J. Kocin, 1983: An interactive Barnes objective map analysis scheme for use with satellite and conventional data. *J. Climate Appl. Meteor.*, **22**, 1487–1503, https://doi.org/10.1175/1520-0450(1983)022<1487:AIBOMA>2.0.CO;2.

Kosiba, K., J. Wurman, Y. Richardson, P. Markowski, P. Robinson, and J. Marquis, 2013: Genesis of the Goshen County, Wyoming, Tornado on 5 June 2009 during VORTEX2. *Mon. Wea. Rev.*, **141**, 1157–1181, https://doi.org/10.1175/MWR-D-12-00056.1.

Kumjian, M. R., and A. V. Ryzhkov, 2008: Polarimetric signatures in supercell thunderstorms. *J. Appl. Meteor. Climatol.*, **47**, 1940–1961, https://doi.org/10.1175/2007JAMC1874.1.

Kurdzo, J. M., D. J. Bodine, B. L. Cheong, and R. D. Palmer, 2015: High-temporal resolution polarimetric X-band Doppler radar observations of the 20 May 2013 Moore, Oklahoma, tornado. *Mon. Wea. Rev.*, **143**, 2711–2735, https://doi.org/10.1175/MWR-D-14-00357.1.

——, and Coauthors, 2017: Observations of severe local storms and tornadoes with the atmospheric imaging radar. *Bull. Amer. Meteor. Soc.*, **98**, 915–935, https://doi.org/10.1175/BAMS-D-15-00266.1.

Lewellen, D. C., B. Gong, and W. S. Lewellen, 2008: Effects of finescale debris on near-surface tornado dynamics. *J. Atmos. Sci.*, **65**, 3247–3262, https://doi.org/10.1175/2008JAS2686.1.

Mahre, A., J. M. Kurdzo, D. J. Bodine, C. B. Griffin, R. D. Palmer, and T.-Y. Yu, 2018: Analysis of the 16 May 2015 Tipton, Oklahoma, EF-3 tornado at high spatiotemporal resolution using the atmospheric imaging radar. *Mon. Wea. Rev.*, **146**, 2103–2124, https://doi.org/10.1175/MWR-D-17-0256.1.

Majcen, M., P. Markowski, Y. Richardson, D. Dowell, and J. Wurman, 2008: Multipass objective analyses of Doppler radar data. *J. Atmos. Oceanic Technol.*, **25**, 1845–1858, https://doi.org/10.1175/2008JTECHA1089.1.

Oye, R., C. Mueller, and S. Smith, 1995: Software for radar translation, visualization, editing, and interpolation. Preprints, *27th Conf. on Radar Meteorology*, Vail, CO, Amer. Meteor. Soc., 359–363.

Pauley, P., and X. Wu, 1990: The theoretical, discrete, and actual response of the Barnes objective analysis scheme for one- and two-dimensional fields. *Mon. Wea. Rev.*, **118**, 1145–1164, https://doi.org/10.1175/1520-0493(1990)118<1145:TTDAAR>2.0.CO;2.

Pazmany, A. L., J. B. Mead, H. B. Bluestein, J. C. Snyder, and J. B. Houser, 2013: A mobile rapid-scanning X-band polarimetric (RaXPol) Doppler radar system. *J. Atmos. Oceanic Technol.*, **30**, 1398–1413, https://doi.org/10.1175/JTECH-D-12-00166.1.

Rotunno, R., and J. B. Klemp, 1982: The influence of the shear-induced pressure gradient on thunderstorm motion. *Mon. Wea. Rev.*, **110**, 136–151, https://doi.org/10.1175/1520-0493(1982)110<0136:TIOTSI>2.0.CO;2.

——, and J. Klemp, 1985: On the rotation and propagation of simulated supercell thunderstorms. *J. Atmos. Sci.*, **42**, 271–292, https://doi.org/10.1175/1520-0469(1985)042<0271:OTRAPO>2.0.CO;2.

Ryzhkov, A. V., D. S. Zrnić, J. C. Hubbert, V. N. Bringi, J. Vivekanandan, and E. A. Brandes, 2002: Polarimetric radar observations and interpretation of co-cross-polar correlation coefficients. *J. Atmos. Oceanic Technol.*, **19**, 340–354, https://doi.org/10.1175/1520-0426-19.3.340.

——, T. J. Schuur, D. W. Burgess, and D. S. Zrnić, 2005: Polarimetric tornado detection. *J. Appl. Meteor.*, **44**, 557–570, https://doi.org/10.1175/JAM2235.1.

Salazar-Cerreno, J. L., and Coauthors, 2017: Development of a mobile C-band Polarimetric Atmospheric Imaging Radar (PAIR). *Special Symp. on Meteorological Observations and Instrumentation*, Seattle, WA, Amer. Meteor. Soc., 1B.1, https://ams.confex.com/ams/97Annual/webprogram/Paper308655.html.

Schultz, C. J., W. A. Petersen, and L. D. Carey, 2012: Dual-polarization tornadic debris signatures. Part I: Examples and utility in an operational setting. *Electron. J. Oper. Meteor.*, **13**, 120–137.

Shapiro, A., K. M. Willingham, and C. K. Potvin, 2010: Spatially variable advection correction of radar data. Part I: Theoretical considerations. *J. Atmos. Sci.*, **67**, 3445–3456, https://doi.org/10.1175/2010JAS3465.1.

Snyder, J. C., and H. B. Bluestein, 2014: Some considerations for the use of high-resolution mobile radar data in tornado intensity determination. *Wea. Forecasting*, **29**, 799–827, https://doi.org/10.1175/WAF-D-14-00026.1.

——, ——, G. Zhang, and S. J. Frasier, 2010: Attenuation correction and hydrometeor classification of high-resolution, X-band, dual-polarized mobile radar measurements in severe convective storms. *J. Atmos. Oceanic Technol.*, **27**, 1979–2001, https://doi.org/10.1175/2010JTECHA1356.1.

——, ——, V. Venkatesh, and S. J. Frasier, 2013: Observations of polarimetric signatures in supercells by an X-band mobile Doppler radar. *Mon. Wea. Rev.*, **141**, 3–29, https://doi.org/10.1175/MWR-D-12-00068.1.

Tanamachi, R. L., H. B. Bluestein, J. B. Houser, S. J. Frasier, and K. M. Hardwick, 2012: Mobile, X-band, polarimetric Doppler radar observations of the 4 May 2007 Greensburg, Kansas, tornadic supercell. *Mon. Wea. Rev.*, **140**, 2103–2125, https://doi.org/10.1175/MWR-D-11-00142.1.

——, ——, M. Xue, W.-C. Lee, K. A. Orzel, S. J. Frasier, and R. M. Wakimoto, 2013: Near-surface vortex structure in a tornado and in a sub-tornado-strength convective-storm vortex observed by a mobile, W-band radar during VORTEX2. *Mon. Wea. Rev.*, **141**, 3661–3690, https://doi.org/10.1175/MWR-D-12-00331.1.

Thompson, R. L., R. Edwards, and J. A. Hart, 2002: Evaluation and interpretation of the supercell composite and significant tornado parameters at the Storm Prediction Center. Preprints, *21st Conf. on Severe Local Storms*, San Antonio, TX, Amer. Meteor. Soc., J3.2, https://ams.confex.com/ams/SLS_WAF_NWP/techprogram/paper_46942.htm.

——, C. M. Mead, and R. Edwards, 2007: Effective storm-relative helicity and bulk shear in supercell thunderstorm environments. *Wea. Forecasting*, **22**, 102–115, https://doi.org/10.1175/WAF969.1.

Torres, S., and C. Curtis, 2006: Initial implementation of super-resolution data on the NEXRAD network. Preprints, *Third European Conf. on Radar Meteorology and Hydrology (ERAD)*, Barcelona, Spain, Amer. Meteor. Soc., 5B.10, https://ams.confex.com/ams/pdfpapers/116240.pdf.

Umeyama, A., B. L. Cheong, S. Torres, and D. Bodine, 2018: Orientation analysis of simulated tornadic debris. *J. Atmos. Oceanic Technol.*, **35**, 993–1010, https://doi.org/10.1175/JTECH-D-17-0140.1.

Van Den Broeke, M. S., 2015: Polarimetric tornadic debris signature variability and debris fallout signatures. *J. Appl. Meteor. Climatol.*, **54**, 2389–2405, https://doi.org/10.1175/JAMC-D-15-0077.1.

——, and S. T. Jauernic, 2014: Spatial and temporal characteristics of polarimetric tornadic debris signatures. *J. Appl. Meteor. Climatol.*, **53**, 2217–2231, https://doi.org/10.1175/JAMC-D-14-0094.1.

Wakimoto, R. M., Z. Wienhoff, H. B. Bluestein, and D. Reif, 2018: The Dodge City tornadoes on 24 May 2016: Damage survey, photogrammetric analysis combined with mobile polarimetric radar data. *Mon. Wea. Rev.*, **146**, 3735–3771, https://doi.org/10.1175/MWR-D-18-0125.1.

——, ——, ——, D. J. Bodine, and J. M. Kurdzo, 2020: Mobile radar observations of the evolving debris field compared with a damage survey of the Shawnee, Oklahoma, tornado of 19 May 2013. *Mon. Wea. Rev.*, **148**, 1779–1803, https://doi.org/10.1175/MWR-D-19-0215.1.

Wienhoff, Z. B., and Coauthors, 2018: Applications of a spatially variable advection correction technique for temporal correction of dual-Doppler analyses of tornadic supercells. *Mon. Wea. Rev.*, **146**, 2949–2971, https://doi.org/10.1175/MWR-D-17-0360.1.

Wurman, J., and M. Randall, 2001: An inexpensive, mobile, rapid-scan radar. Preprints, *30th Conf. on Radar Meteorology*, Munich, Germany, Amer. Meteor. Soc., P3.4, https://ams.confex.com/ams/30radar/techprogram/paper_21577.htm.

——, J. Straka, E. Rasmussen, M. Randall, and A. Zahrai, 1997: Design and deployment of a portable, pencil-beam, pulsed, 3-cm Doppler radar. *J. Atmos. Oceanic Technol.*, **14**, 1502–1512, https://doi.org/10.1175/1520-0426(1997)014<1502:DADOAP>2.0.CO;2.